

**SYNTHESIS AND EVALUATION OF POLY
(ETHYLENE) OXIDE/ERBIUM OXIDE AS
POTENTIAL DIAGNOSTIC NANOFIBRES FOR
MAGNETIC RESONANCE IMAGING**

MUNIRAH BINTI JAMIL

UNIVERSITI SAINS MALAYSIA

2023

**SYNTHESIS AND EVALUATION OF POLY
(ETHYLENE) OXIDE/ERBIUM OXIDE AS
POTENTIAL DIAGNOSTIC NANOFIBRES FOR
MAGNETIC RESONANCE IMAGING**

by

MUNIRAH BINTI JAMIL

**Thesis submitted in fulfilment of the requirements
for the degree of
Doctor of Philosophy**

September 2023

ACKNOWLEDGEMENT

Alhamdulillah, I have overcome endless obstacles and hardships since the 1st year of PhD studies in March 2017 while caring for sick family members and finally completed my studies with flying colours. I acknowledged the challenges of doing laboratory work during the Covid-19 outbreaks in March 2020 despite officially starting my new research in the 6th semester on January 8, 2020, with a new supervisory committee. I feel blessed and grateful because Allah S.W.T. has eased everything for me by sending countless people at the right time whenever I seek help. Indeed, patience and the power of du'a can overcome everything. I spent 328 days on laboratory work and a semester completing my dissertation and journal publications. I am deeply indebted to my parents (Wazirah binti Hassan & Jamil bin Yusop), my siblings (Ahmad Mahfooz bin Jamil, Amirah binti Jamil, Ahmad Afeeq bin Jamil & Siti Aisyah binti Jamil), and relatives (Zainuriah binti Haasan, Muhammad Hafiz bin Hassan & Muhammad Zahir bin Hassan), who have endlessly inspired and stood with me through my most challenging times with unconditional love, understanding and assistance throughout my studies. Resting since December 8, 2021, my late grandmother (Allahyarhamah Salbiah binti Abdullah) was a steadfast source of encouragement during my PhD journey. She provided unwavering support and earnest prayers for my success and always reminded me to persist in facing challenges. I am grateful to have my best friends (Fahimah Nadiyah binti Mohd Ariff & Afrina binti Mohd Nasir) and beloved companions (Oliver Benjamin, Chimmie Changga, Mochie, Jewel, Chuzzle, Marmalade, Mandoo, Domino, Koda, Chantique, Chestnut, Dobby Botswana, Bagheera, Baloo, Peekka, Fettuccini, An An, Chamchim, Whoopie, Popoya, Chummie, Chombie, Mowgly, Bilbo, Popoye, Diego, Daegu, Commot, Bella, Onnie,

Sven & Achoo), who were always with me during my most challenging time. This endeavour would not have been possible without the guidance and encouragement of my supervisors (Assoc. Prof. Dr Iskandar Shahrin bin Mustafa, Assoc. Prof. Dr Naser Mahmoud Ahmed & Assoc. Prof. Dr Datin Shahrul Bariyah binti Sahul Hamid), who constantly supervised me, shared their expertise and assisted me throughout the research. I was exceptionally grateful to the School of Physics for the financial support to cover the tuition fees in the 3rd year and to the ZAWAIN for supporting the living expenses because the funding alleviated my financial constraints that year. Moreover, I was fortunate to have had experience as a part-time research assistant and had the opportunity to become a graduate research assistant. I sincerely thank my enthusiastic teammates (Hanisha binti Mohd Shariff, Thair Hussien Khaazalah, Nabasu Seth Ezra, Efenji Godwin Irinam & Hayder Salah Naeem), who have always shown positivity to boost my confidence. This acknowledgement is also extended to the School of Physics laboratory staff (Mrs Aznorhaida binti Ramli, Mr Mohd Rizal bin Mohamad Rodin, Mr Hazhar bin Hassan, Mrs Ee Bee Choo, Mr Yushamdan bin Yusof, Mrs Mahfuzah binti Mohamad Fuad & Mr Abdul Jamil bin Yusuf) and AMDI Oncology laboratory staff (Mrs Halianis binti Mohd Yusoff, Mrs Ira Maya Sophia binti Nordin & Mr Norhiman bin Ahmad) for their valuable assistance. A special thanks to all who have helped and stayed with me throughout this journey. Lastly, as a lifetime learner, I hope this graduation will be an excellent start to a new life for my dreams and career. Aamiin.

TABLE OF CONTENTS

ACKNOWLEDGEMENT	ii
TABLE OF CONTENTS	iv
LIST OF TABLES	xi
LIST OF FIGURES	xiv
LIST OF SYMBOLS	xxxi
LIST OF ABBREVIATIONS	xxxii
LIST OF APPENDICES	xxxvi
ABSTRAK	xxxvii
ABSTRACT	xxxix
CHAPTER 1 INTRODUCTION	1
1.1 Background of the study	1
1.2 Problem statement	5
1.3 Objectives of the study	9
1.4 Scope of the study	10
1.5 Significance of the study.....	11
1.6 Dissertation outline.....	11
CHAPTER 2 THEORY AND LITERATURE REVIEW	13
2.1 Introduction to diagnostic imaging.....	13
2.2 Principles of magnetic resonance imaging (MRI).....	13
2.2.1 T1 longitudinal relaxation time	14
2.2.2 T2 transverse relaxation time	15
2.3 Diagnostic agents	16
2.3.1 Positive (T1) diagnostic agent	19
2.3.2 Negative (T2) diagnostic agent.....	21
2.4 Introduction to electrospinning	23

2.5	Principles of electrospinning system	24
2.6	Parameters influencing the electrospinning process	26
2.6.1	ES setting parameters	26
2.6.1(a)	Applied high voltage	26
2.6.1(b)	Spinneret diameter	27
2.6.1(c)	The distance from the spinneret tip to the collector	27
2.6.1(d)	Flow rate	28
2.6.2	Solution parameters.....	29
2.6.2(a)	Polymer concentration.....	29
2.6.2(b)	Viscosity	29
2.6.2(c)	Conductivity	30
2.6.2(d)	Surface tension.....	31
2.6.2(e)	Solvent volatility	31
2.6.3	Environmental parameters.....	32
2.6.3(a)	Temperature	32
2.6.3(b)	Relative humidity	32
2.7	Nanofibres for bioimaging applications	33
2.8	Biocompatible polymer	36
2.8.1	Poly (ethylene) oxide	37
2.9	Lanthanide.....	38
2.9.1	Erbium oxide	39
2.10	Nanoparticles	40
2.10.1	Mechanisms of nanoparticle toxicity	41
2.11	MCF-7 breast cancer cell line	42
2.11.1	Morphology of MCF-7 cells.....	44
2.11.2	<i>In vitro</i> study of MCF-7 cells	44

CHAPTER 3	MATERIALS AND METHODS	47
3.1	Introduction.....	47
3.2	Materials and apparatus	47
3.3	Part 1: PEO nanofibres	48
3.3.1	Preparation of poly (ethylene) oxide (PEO) polymer blends	48
3.3.2	Viscosity test.....	48
3.3.3	Fabrication of poly (ethylene) oxide (PEO) nanofibres.....	48
3.3.4	Morphology of PEO nanofibres.....	50
	3.3.4(a) Fibre diameter and thickness	50
	3.3.4(b) Surface roughness	50
3.3.5	Surface chemistry of PEO nanofibres	51
3.3.6	Release profile of PEO nanofibres.....	51
3.3.7	Cell culture	52
	3.3.7(a) Preparation of DMEM complete media	53
	3.3.7(b) Thawing frozen cells	53
	3.3.7(c) Cell seeding and cell culture.....	54
	3.3.7(d) Trypsinisation	55
	3.3.7(e) Cryopreservation of cells.....	56
	3.3.7(f) Cell count using a haemocytometer	56
	3.3.7(g) Preparation of nanofibre stock for cell treatment	57
3.3.8	MTS cell proliferation assay	59
3.3.9	Colony formation assay.....	60
3.3.10	Statistical analysis.....	62
3.4	Part 2: PEO/Er ₂ O ₃ nanofibres	62
3.4.1	Preliminary study of synthesised PEO/Er ₂ O ₃ nanofibres.....	62
3.4.2	Zeta potential and particle stability of erbium oxide (Er ₂ O ₃) nanoparticles and synthesised PEO/Er ₂ O ₃ nanofibres	63

3.4.3	Preparation of poly (ethylene) oxide/erbium oxide (PEO/Er ₂ O ₃) polymer blends.....	64
3.4.4	Fabrication of poly (ethylene) oxide/erbium oxide (PEO/Er ₂ O ₃) nanofibres	64
3.4.5	Morphology of PEO/Er ₂ O ₃ nanofibres.....	65
	3.4.5(a) Fibre diameter and thickness	66
	3.4.5(b) Surface roughness	67
	3.4.5(c) Er ₂ O ₃ nanoparticles morphology	68
3.4.6	Entrapment efficiency of PEO/Er ₂ O ₃ nanofibres	68
3.4.7	Physical properties of PEO/Er ₂ O ₃ nanofibres	69
	3.4.7(a) Surface chemistry.....	69
	3.4.7(b) Crystalline phase and structure	70
3.4.8	Release profile of PEO/Er ₂ O ₃ nanofibres.....	71
3.4.9	MTS cell proliferation assay	72
3.4.10	Colony formation assay.....	72
3.4.11	Functional analysis of PEO/Er ₂ O ₃ nanofibre uptake by the MCF-7 cells	73
	3.4.11(a) Preparation of cell fixation	73
	3.4.11(b) Preparation of processing block.....	74
	3.4.11(c) Sectioning and ultramicrotomy.....	77
	3.4.11(d) Cells staining and viewing process	80
3.5	Part 3: MRI and <i>in vitro</i> MRI.....	81
3.6	Statistical analysis	85
3.7	Summary of the methodology.....	86
	3.7.1 Part 1 (PEO nanofibres)	86
	3.7.2 Part 2 (PEO/Er ₂ O ₃ nanofibres)	87
	3.7.3 Part 3 (MRI and <i>in vitro</i> MRI).....	88

CHAPTER 4	RESULTS AND DISCUSSION	89
4.1	Introduction.....	89
4.2	Part 1: Preliminary studies.....	89
4.2.1	Viscosity of PEO polymer blends.....	90
4.2.2	Morphology of PEO nanofibres.....	91
4.2.2(a)	PEO fibre diameter.....	93
4.2.2(b)	PEO fibre thickness.....	94
4.2.3	Surface roughness of PEO nanofibres.....	96
4.2.4	Surface chemistry of PEO nanofibres	98
4.2.5	Release profile and stability of PEO nanofibres.....	100
4.2.6	Cell culture	102
4.2.7	Effects of PEO nanofibres in MCF-7 cells cytotoxicity	103
4.2.8	Colony formation assay.....	106
4.2.8(a)	Optimisation of colony formation assay	106
4.2.8(b)	Effects of PEO nanofibres in MCF-7 cells clonogenicity.....	107
4.3	Part 2: Potential usage	109
4.3.1	Effects of surfactant on the morphology of synthesised PEO/Er ₂ O ₃ nanofibres.....	110
4.3.2	Effects of synthesised PEO/Er ₂ O ₃ nanofibres on zeta potential and particle stability	114
4.3.3	Morphology of PEO/Er ₂ O ₃ nanofibres.....	116
4.3.3(a)	Batch A – PEO with low concentrations of Er ₂ O ₃ nanoparticles formulation.....	117
4.3.3(b)	Batch B – PEO with high concentrations of Er ₂ O ₃ nanoparticles formulation.....	124
4.3.4	Morphology of Er ₂ O ₃ nanoparticles in the PEO matrix.....	133
4.3.5	Entrapment efficiency of PEO/Er ₂ O ₃ nanofibres	135
4.3.6	Surface roughness of PEO/Er ₂ O ₃ nanofibres	136

4.3.6(a)	Batch A – PEO with low concentrations of Er ₂ O ₃ nanoparticles formulation.....	137
4.3.6(b)	Batch B – PEO with high concentrations of Er ₂ O ₃ nanoparticles formulation.....	139
4.3.7	Surface chemistry of PEO/Er ₂ O ₃ nanofibres.....	141
4.3.8	Crystalline phase structure of PEO/Er ₂ O ₃ nanofibres.....	143
4.3.8(a)	Batch A – PEO with low concentrations of Er ₂ O ₃ nanoparticles formulation.....	143
4.3.8(b)	Batch B – PEO with high concentrations of Er ₂ O ₃ nanoparticles formulation.....	147
4.3.9	Release profile and stability of PEO/Er ₂ O ₃ nanofibres.....	149
4.3.9(a)	Batch A – PEO with low concentrations of Er ₂ O ₃ nanoparticles formulation.....	149
4.3.9(b)	Batch B – PEO with high concentrations of Er ₂ O ₃ nanoparticles formulation.....	152
4.3.10	Effects of Er ₂ O ₃ nanoparticles and PEO/Er ₂ O ₃ nanofibres in MCF-7 cells cytotoxicity.....	154
4.3.10(a)	Batch A – PEO with low concentrations of Er ₂ O ₃ nanoparticles formulation.....	154
4.3.10(b)	Batch B – PEO with high concentrations of Er ₂ O ₃ nanoparticles formulation.....	158
4.3.11	Effects of Er ₂ O ₃ nanoparticles and PEO/Er ₂ O ₃ nanofibres in MCF-7 cells clonogenicity.....	161
4.3.11(a)	Batch A – PEO with low concentrations of Er ₂ O ₃ nanoparticles formulation.....	161
4.3.11(b)	Batch B – PEO with high concentrations of Er ₂ O ₃ nanoparticles formulation.....	163
4.3.12	Effects of Er ₂ O ₃ nanoparticles' uptake on cellular morphology and its distribution.....	165
4.3.12(a)	Batch A – PEO with low concentrations of Er ₂ O ₃ nanoparticles formulation.....	165
4.3.12(b)	Batch B – PEO with high concentrations of Er ₂ O ₃ nanoparticles formulation.....	169
4.4	Part 3: MRI applications.....	172

4.4.1	Performance of PEO/Er ₂ O ₃ nanofibres as MRI diagnostic nanofibres	173
4.4.1(a)	Batch A – PEO with low concentrations of Er ₂ O ₃ nanoparticles formulation.....	173
4.4.1(b)	Batch B – PEO with high concentrations of Er ₂ O ₃ nanoparticles formulation.....	184
4.4.2	Performance of PEO/Er ₂ O ₃ nanofibres as <i>in vitro</i> MRI diagnostic nanofibres	197
4.4.2(a)	Batch A – PEO with low concentrations of Er ₂ O ₃ nanoparticles formulation.....	197
4.4.2(b)	Batch B – PEO with high concentrations of Er ₂ O ₃ nanoparticles formulation.....	208
4.4.2(c)	Sensitivity of the P.Er4 formulation at 10 µg/ml dose concentration as a T1-T2 dual-mode diagnostic nanofibre.....	221
CHAPTER 5 CONCLUSION AND FUTURE RECOMMENDATIONS		225
5.1	Conclusion	225
5.2	Recommendations for future research.....	226
REFERENCES		228
APPENDICES		
LIST OF PUBLICATIONS		

LIST OF TABLES

		Page
Table 2.1	Frequent use of standard hypodermic needle diameter for electrospinning.	27
Table 2.2	Types of phase separation method as one of the solvent volatility factors in the electrospinning process.	32
Table 2.3	Types of receptors in the breast cancer cell line.	43
Table 3.1	PEO polymer blend formulations for fabricating nanofibre mats.	48
Table 3.2	Electrospinning setting for the fabrication of different PEO nanofibre formulations.	50
Table 3.3	Stock preparation for cell culture experiment.	58
Table 3.4	Preliminary experimental composition of polymer blend formulations in v/v% ratio.	63
Table 3.5	Final experimental composition of polymer blend formulations in v/v% ratio.	64
Table 3.6	Electrospinning setting for fabricating different PEO/Er ₂ O ₃ nanofibre formulations.	65
Table 3.7	Steps of block processing preparation.	76
Table 3.8	Process of sectioning and ultramicrotomy.	80
Table 4.1	Composition of PEO polymer blend formulations in wt% ratio.	90
Table 4.2	Wavenumbers and assignments of IR bands from PEO nanofibres. Where ν = stretch, δ = scissor/deformation, ω = wag, and ρ = rock, τ = twist. The subscript "as" refers to asymmetric vibrational mode.	100
Table 4.3	Comparison between the number of colonies after treatment with different formulations of PEO nanofibres.	107

Table 4.4	Preliminary experimental composition of polymer blend formulations in v/v% ratio.....	110
Table 4.5	Zeta potential of Er ₂ O ₃ nanoparticles and synthesised PEO/Er ₂ O ₃ nanofibres.....	114
Table 4.6	The entrapment efficiency of Er ₂ O ₃ nanoparticles in PEO nanofibres.....	136
Table 4.7	Wavenumbers and assignments of IR bands from PEO and PEO/Er ₂ O ₃ nanofibres. Where ν = stretch, δ = scissor/deformation, ω = wag, ρ = rock, and τ = twist. The subscripts “s” and “as” refer to symmetric and asymmetric vibrational modes.....	143
Table 4.8	Summary of d-spacing and crystallite size of PEO/Er ₂ O ₃ nanofibres in Batch A.....	145
Table 4.9	Summary of d-spacing and crystallite size of PEO/Er ₂ O ₃ nanofibres in Batch B.....	148
Table 4.10	Comparison between the number of colonies after treatment with different formulations of PEO/Er ₂ O ₃ nanofibres in Batch A.....	162
Table 4.11	Comparison between the number of colonies after treatment with different formulations of PEO/Er ₂ O ₃ nanofibres in Batch B.....	164
Table 4.12	Comparison of r_2/r_1 ratio between Er ₂ O ₃ nanoparticles (negative control) and PEO/Er ₂ O ₃ nanofibres in Batch A.....	183
Table 4.13	Comparison of r_2/r_1 ratio between Er ₂ O ₃ nanoparticles (negative control) and PEO/Er ₂ O ₃ nanofibres in Batch B.....	195
Table 4.14	Comparison of r_2/r_1 ratio between treated cells with Er ₂ O ₃ nanoparticles (negative control) and treated cells with PEO/Er ₂ O ₃ nanofibres in Batch A.....	207
Table 4.15	Comparison of r_2/r_1 ratio between treated cells with Er ₂ O ₃ nanoparticles (negative control) and treated cells with PEO/Er ₂ O ₃ nanofibres in Batch B.....	217
Table 4.16	Paired t-tests of the signal intensity between each TR setting for T1-weighted images and TE setting for T2-weighted images at 10	

$\mu\text{g/ml}$ dose of the P.Er4 formulation normalised to untreated cells
(positive control)..... 224

LIST OF FIGURES

	Page
Figure 2.1	Schematic diagram of T1 longitudinal relaxation time after applying 90° RF pulse to the MRI system at equilibrium. The net magnetisation vector of the z-axis (M_z) is reduced to zero but gradually returns to its equilibrium value without the RF pulse (Caspani et al., 2020). 15
Figure 2.2	Schematic diagram of T2 transverse relaxation time after applying 90° RF pulse to the MRI system at equilibrium. Initially, the transverse magnetisation (red arrow) has a maximum amplitude as the population of magnetic moments rotates in phase towards the xy plane. The amplitude of the net transverse magnetisation decays without the RF pulse. Free Induction Decay (FID) is the resultant decay signal (Caspani et al., 2020). 16
Figure 2.3	Schematic illustration of the conventional electrospinning (ES) setup and its variable parameters (Long et al., 2018). 24
Figure 2.4	Morphology of human breast adenocarcinoma (MCF-7 cells) (Mabeta et al., 2018). 44
Figure 3.1	Schematic illustration of the electrospinning process in fabricating nanofibre mats. 49
Figure 3.2	Schematic diagram of the fibre release profile protocol using UV-Vis spectroscopy. 52
Figure 3.3	DMEM complete media was prepared and stored in the refrigerator at 4°C for cell culture experiments. 53
Figure 3.4	Seeded cells for cell culture experiment viewed at 200x magnification. At this stage, cells appeared spherical and floating in the culture media. 54
Figure 3.5	MCF-7 cell culture using DMEM complete media indicates the cell growth by colour changes. 55

Figure 3.6	MCF-7 cell line kept in cryovials and stored inside a liquid nitrogen tank at -196°C for cell preservation.	56
Figure 3.7	Cell count viewed under an inverted phase-contrast microscope at 50x magnification. The cells inside the 16 small squares were counted.	57
Figure 3.8	Stocks prepared for use in the cell culture assays.	58
Figure 3.9	Schematic diagram of the MTS cell proliferation assay protocol.	60
Figure 3.10	Schematic diagram of the colony formation assay protocol.	62
Figure 3.11	The electrospinning setup for nanofibre mat fabrication.	65
Figure 3.12	FESEM system (Nova NanoSEM 450, USA) offers a detailed view of the fibre morphology.	66
Figure 3.13	Sputter coater (Quorum Q150R S) provides a platinum coating on the nanofibre's surface to reduce the charging effect during observation.	67
Figure 3.14	Atomic force microscopy (AFM) (Bruker Dimension Edge) offers a detailed view of the surface roughness of the nanofibres.	68
Figure 3.15	Inductively coupled plasma-optical emission spectrometry (ICP-OES) (Agilent Technologies 700 Series) offers detailed information on the loading of Er ₂ O ₃ nanoparticles in the PEO matrix.	69
Figure 3.16	Fourier transform infrared (FTIR) spectroscopy (PerkinElmer Spectrum GX) provides insight into the surface chemistry of nanofibres.	70
Figure 3.17	X-ray diffractometer (XRD) (PANalytical X'Pert PRO) offers detailed information on the crystalline phase and structure of PEO/Er ₂ O ₃ nanofibres.	70
Figure 3.18	Treated cells suspended in McDowell Trump fixative stored in the refrigerator at 4°C overnight.	74
Figure 3.19	The cube specimen was suspended in a vial containing 50% ethanol before proceeding to the serial dehydration procedure.	75

Figure 3.20	The resin block samples after being cured at 60°C in the oven overnight.	76
Figure 3.21	A fine trimming of resin block sample using a glass knife under a cutting microscope (PowerTome XL RMC).....	77
Figure 3.22	Preparation of knife boat for a sectioning procedure.....	78
Figure 3.23	Schematic diagram of the semi-thin sectioning process.	78
Figure 3.24	The colour reference chart for ultramicrotome sections.	79
Figure 3.25	Fabricated samples in 1% agarose gel for MRI and <i>in vitro</i> MRI experiments.	82
Figure 3.26	The position of fabricated samples before scanning under MRI 1.5 Tesla.....	83
Figure 3.27	Part 1 (PEO nanofibres) methodology flowchart.	86
Figure 3.28	Part 2 (PEO/Er ₂ O ₃ nanofibres) methodology flowchart.	87
Figure 3.29	Part 3 (MRI and <i>in vitro</i> MRI) methodology flowchart.	88
Figure 4.1	Viscosity of poly (ethylene) oxide (PEO) polymer blends with different formulations.	90
Figure 4.2	Fibre morphology of PEO nanofibres with different formulations observed under FESEM at 50kx magnification. (a) P4 is 4 wt% PEO nanofibre, (b) P5 is 5 wt% PEO nanofibre, (c) P6 is 6 wt% PEO nanofibre and (d) P7 is 7 wt% PEO nanofibre.....	92
Figure 4.3	Fibre diameter distributions of PEO nanofibres with different formulations. (a) P5 is 5 wt% PEO nanofibre, (b) P6 is 6 wt% PEO nanofibre and (c) P7 is 7 wt% PEO nanofibre.	93
Figure 4.4	The thickness of PEO nanofibres with different formulations observed under FESEM at 100x magnification. The red arrow indicates the fibre thickness. (a) P4 is 4 wt% PEO nanofibre, (b) P5 is 5 wt% PEO nanofibre and (c) P6 is 6 wt% PEO nanofibre and (d) P7 is 7 wt% PEO nanofibre.....	95
Figure 4.5	Average fibre thickness of PEO nanofibres with different formulations. The nanofibre formulation of P4 is 4 wt% PEO	

	nanofibre, P5 is 5 wt% PEO nanofibre, P6 is 6 wt% PEO nanofibre and P7 is 7 wt% PEO nanofibre. All experiments were performed in triplicate (n = 3). The asterisk (***) indicates a significant difference with $p < 0.000$	96
Figure 4.6	3D images of surface roughness and profile of PEO nanofibres with different formulations. (a) P4 is 4 wt% PEO nanofibre, (b) P5 is 5 wt% PEO nanofibre, (c) P6 is 6 wt% PEO nanofibre and (d) P7 is 7 wt% PEO nanofibre.....	97
Figure 4.7	Average surface roughness (R_a) of PEO nanofibres with different formulations. The nanofibre formulation of P4 is 4 wt% PEO nanofibre, P5 is 5 wt% PEO nanofibre, P6 is 6 wt% PEO nanofibre and P7 is 7 wt% PEO nanofibre. All experiments were performed in triplicate (n =3). The asterisk (**) indicates a significant difference with $p < 0.01 - 0.001$	98
Figure 4.8	FTIR spectra and pertinent band distributions of PEO nanofibres with different formulations. The nanofibre formulation of P4 is 4 wt% PEO nanofibre, P5 is 5 wt% PEO nanofibre, P6 is 6 wt% PEO nanofibre and P7 is 7 wt% PEO nanofibre.	99
Figure 4.9	Release profile of the PEO nanofibres with different formulations. The nanofibre formulation of P4 is 4 wt% PEO nanofibre, P5 is 5 wt% PEO nanofibre, P6 is 6 wt% PEO nanofibre, and P7 is 7 wt% PEO nanofibre.	101
Figure 4.10	MCF-7 cell growth inside T25 flask at 100x magnification. (a) Cells appeared spherical and floating after thawing from liquid nitrogen. (b) Adherent cells after 3 days of incubation. (c) Cells gained epithelial shape after 7 days at 100x magnification. (d) Confluence MCF-7 cells viewed at 200x magnification.	102
Figure 4.11	Dose-response curve with different poly (ethylene) oxide (PEO) concentrations tested in the MCF-7 cells: (a) Low dose concentrations from 10 – 100 $\mu\text{g/ml}$ and (b) High dose concentrations from 100 – 1000 $\mu\text{g/ml}$. The nanofibre formulation of P5 is 5 wt% PEO nanofibre, P6 is 6 wt% PEO nanofibre and P7	

	is 7 wt% PEO nanofibre. All experiments were performed in triplicate (n = 3). The asterisk (*) indicates a significant difference with $p < 0.05 - 0.01$, (**) indicates a significant difference with $p < 0.01 - 0.001$ and (***) indicates a significant difference with $p < 0.000$	104
Figure 4.12	Number of colonies formed after 9 days of treatment. All experiments were performed in triplicate (n = 3). The asterisk (*) indicates a significant difference with $p < 0.05 - 0.01$	106
Figure 4.13	Number of colonies formed after 9 days of treatment. All experiments were performed in triplicate (n = 3). The asterisk (*) indicates a significant difference with $p < 0.05 - 0.01$, and (**) indicates a significant difference with $p < 0.01 - 0.001$	108
Figure 4.14	Fibre morphology of the synthesised PEO/Er ₂ O ₃ nanofibres with different ratios of Er ₂ O ₃ nanoparticles to SDS concentrations at 15kx magnification. (a) PEO/Er ₂ O ₃ nanofibre without the addition of SDS. The ratio of Er ₂ O ₃ to 1 mM SDS: (b) 1:1, (c) 1:2, (d) 2:1. The ratio of Er ₂ O ₃ to 1.5 mM SDS: (e) 2:1.	112
Figure 4.15	Schematic illustration of the ionic interaction between PEO and Er ₂ O ₃ nanoparticles. PEO had a higher concentration in the colloidal dispersion than Er ₂ O ₃ nanoparticles. The negative charges from carboxylic terminal groups in PEO resulted in an elevated negative zeta potential for the PEO/Er ₂ O ₃ nanofibres.	115
Figure 4.16	Fibre morphology of PEO/Er ₂ O ₃ nanofibres in Batch A observed using SE and BSE techniques at 50kx magnification complemented with EDX spectra. EDX showed Er ₂ O ₃ nanoparticles as the elemental component in the fibre. Other peaks detected were C and O derived from the polymer structure of PEO [(-CH ₂ CH ₂ O-) _n], which was the host of the nanofibre material. (a) P.Er2 is a nanofibre formulation of PEO with 2 v/v% Er ₂ O ₃ nanoparticles. (b) P.Er4 is a nanofibre formulation of PEO with 4 v/v% Er ₂ O ₃ nanoparticles. (c) P.Er6 is a nanofibre formulation of	

- PEO with 6 v/v% Er₂O₃ nanoparticles. (d) **P.Er8** is a nanofibre formulation of PEO with 8 v/v% Er₂O₃ nanoparticles..... 118
- Figure 4.17 Fibre diameter distributions of PEO/Er₂O₃ nanofibres in Batch A. (a) **P.Er2** is a nanofibre formulation of PEO with 2 v/v% Er₂O₃ nanoparticles. (b) **P.Er4** is a nanofibre formulation of PEO with 4 v/v% Er₂O₃ nanoparticles. (c) **P.Er6** is a nanofibre formulation of PEO with 6 v/v% Er₂O₃ nanoparticles. (d) **P.Er8** is a nanofibre formulation of PEO with 8 v/v% Er₂O₃ nanoparticles..... 120
- Figure 4.18 The thickness of PEO/Er₂O₃ nanofibres with different formulations in Batch A observed under FESEM at 500x magnification. The red arrow indicates the fibre thickness. (a) **P.Er2** is a nanofibre formulation of PEO with 2 v/v% Er₂O₃ nanoparticles. (b) **P.Er4** is a nanofibre formulation of PEO with 4 v/v% Er₂O₃ nanoparticles. (c) **P.Er6** is a nanofibre formulation of PEO with 6 v/v% Er₂O₃ nanoparticles. (d) **P.Er8** is a nanofibre formulation of PEO with 8 v/v% Er₂O₃ nanoparticles..... 122
- Figure 4.19 Average fibre thickness of PEO/Er₂O₃ nanofibres in Batch A. The nanofibre formulation of **P.Er2** is PEO with 2 v/v% Er₂O₃ nanoparticles, **P.Er4** is PEO with 4 v/v% Er₂O₃ nanoparticles, **P.Er6** is PEO with 6 v/v% Er₂O₃ nanoparticles, and **P.Er8** is PEO with 8 v/v% Er₂O₃ nanoparticles. The asterisk (*) indicates a significant difference with $p < 0.05 - 0.01$, (**) indicates a significant difference with $p < 0.01 - 0.001$, and (***) indicates a significant difference with $p < 0.001 - 0.000$ 123
- Figure 4.20 Schematic illustration of the correlation between fibre diameter and thickness. As demonstrated, the self-assembly of a single nanofibre during electrospinning has piled up to become a nanofibre fibre mat, contributing to the thickness expansion. 124
- Figure 4.21 Fibre morphology of PEO/Er₂O₃ nanofibres in Batch B observed using SE and BSE techniques at 50kx magnification complemented with EDX spectra. EDX showed Er₂O₃ nanoparticles as the elemental component in the fibre. Other peaks

detected were C and O derived from the polymer structure of PEO $[(-CH_2CH_2O-)_n]$, which was the host of the nanofibre material. (a) **P.Er10** is a nanofibre formulation of PEO with 10 v/v% Er_2O_3 nanoparticles. (b) **P.Er15** is a nanofibre formulation of PEO with 15 v/v% Er_2O_3 nanoparticles. (c) **P.Er20** is a nanofibre formulation of PEO with 20 v/v% Er_2O_3 nanoparticles. (d) **P.Er25** is a nanofibre formulation of PEO with 25 v/v% Er_2O_3 nanoparticles..... 126

Figure 4.22 Schematic illustration of the steric interaction of the adsorbed PEO layer in the region between the neighbouring Er_2O_3 nanoparticle surface. 128

Figure 4.23 Fibre diameter distributions of PEO/ Er_2O_3 nanofibres in Batch B. (a) **P.Er10** is a nanofibre formulation of PEO with 10 v/v% Er_2O_3 nanoparticles. (b) **P.Er15** is a nanofibre formulation of PEO with 15 v/v% Er_2O_3 nanoparticles. (c) **P.Er20** is a nanofibre formulation of PEO with 20 v/v% Er_2O_3 nanoparticles. (d) **P.Er25** is a nanofibre formulation of PEO with 25 v/v% Er_2O_3 nanoparticles..... 129

Figure 4.24 The thickness of PEO/ Er_2O_3 nanofibres with different formulations in Batch B observed under FESEM at 500x magnification. The red arrow indicates the fibre thickness. (a) **P.Er10** is a nanofibre formulation of PEO with 10 v/v% Er_2O_3 nanoparticles. (b) **P.Er15** is a nanofibre formulation of PEO with 15 v/v% Er_2O_3 nanoparticles. (c) **P.Er20** is a nanofibre formulation of PEO with 20 v/v% Er_2O_3 nanoparticles. (d) **P.Er25** is a nanofibre formulation of PEO with 25 v/v% Er_2O_3 nanoparticles..... 131

Figure 4.25 Average fibre thickness of PEO/ Er_2O_3 nanofibres in Batch B. The nanofibre formulation of **P.Er10** is PEO with 10 v/v% Er_2O_3 nanoparticles, **P.Er15** is PEO with 15 v/v% Er_2O_3 nanoparticles, **P.Er20** is PEO with 20 v/v% Er_2O_3 nanoparticles, and **P.Er25** is PEO with 25 v/v% Er_2O_3 nanoparticles. All experiments were

	performed in triplicate ($n = 3$). The asterisk (*) indicates a significant difference with $p < 0.05 - 0.01$, (**) indicates a significant difference with $p < 0.01 - 0.001$, and (***) indicates a significant difference with $p < 0.001 - 0.000$	132
Figure 4.26	Morphology of Er_2O_3 nanoparticles embedded in the PEO matrix observed under HRTEM. (a) P.Er4 formulation in Batch A at 43kx and 195kx magnifications. The nanofibre formulation of the P.Er4 is PEO with 4 v/v% Er_2O_3 nanoparticles. (b) P.Er20 formulation in Batch B at 43kx and 97kx magnifications. The nanofibre formulation of the P.Er20 is PEO with 20 v/v% Er_2O_3 nanoparticles.....	134
Figure 4.27	Lattice fringe of PEO/ Er_2O_3 nanofibres and the apparent shape of Er_2O_3 nanoparticles.....	135
Figure 4.28	Size distribution of Er_2O_3 nanoparticles embedded in PEO matrix.	135
Figure 4.29	3D images of surface roughness and profile of PEO/ Er_2O_3 nanofibres in Batch A. (a) P.Er2 is a nanofibre formulation of PEO with 2 v/v% Er_2O_3 nanoparticles. (b) P.Er4 is a nanofibre formulation of PEO with 4 v/v% Er_2O_3 nanoparticles. (c) P.Er6 is a nanofibre formulation of PEO with 6 v/v% Er_2O_3 nanoparticles. (d) P.Er8 is a nanofibre formulation of PEO with 8 v/v% Er_2O_3 nanoparticles.....	137
Figure 4.30	Average surface roughness (R_a) of PEO/ Er_2O_3 nanofibres in Batch A. The nanofibre formulation of P.Er2 is PEO with 2 v/v% Er_2O_3 nanoparticles, P.Er4 is PEO with 4 v/v% Er_2O_3 nanoparticles, P.Er6 is PEO with 6 v/v% Er_2O_3 nanoparticles, and P.Er8 is PEO with 8 v/v% Er_2O_3 nanoparticles. The asterisk (**) indicates a significant difference with $p < 0.01 - 0.001$, and (***) indicates a significant difference with $p < 0.001 - 0.000$	138
Figure 4.31	3D images of surface roughness and profile of PEO/ Er_2O_3 nanofibres in Batch B. (a) P.Er10 is a nanofibre formulation of PEO with 10 v/v% Er_2O_3 nanoparticles. (b) P.Er15 is a nanofibre	

formulation of PEO with 15 v/v% Er₂O₃ nanoparticles. (c) **P.Er20** is a nanofibre formulation of PEO with 20 v/v% Er₂O₃ nanoparticles. (d) **P.Er25** is a nanofibre formulation of PEO with 25 v/v% Er₂O₃ nanoparticles..... 139

Figure 4.32 Average surface roughness of PEO/Er₂O₃ nanofibres in Batch B. The nanofibre formulation of **P.Er10** is PEO with 10 v/v% Er₂O₃ nanoparticles, **P.Er15** is PEO with 15 v/v% Er₂O₃ nanoparticles, **P.Er20** is PEO with 20 v/v% Er₂O₃ nanoparticles, and **P.Er25** is PEO with 25 v/v% Er₂O₃ nanoparticles. The asterisk (*) indicates a significant difference with $p < 0.05 - 0.01$, and (***) indicates a significant difference with $p < 0.001 - 0.000$ 140

Figure 4.33 FTIR spectra and pertinent band distributions of PEO and PEO/Er₂O₃ nanofibres in Batch A and Batch B. The nanofibre formulation of **P5** is 5 wt% PEO, **P.Er2** is PEO with 2 v/v% Er₂O₃ nanoparticles, **P.Er4** is PEO with 4 v/v% Er₂O₃ nanoparticles, **P.Er6** is PEO with 6 v/v% Er₂O₃ nanoparticles, **P.Er8** is PEO with 8 v/v% Er₂O₃ nanoparticles, **P.Er10** is PEO with 10 v/v% Er₂O₃ nanoparticles, **P.Er15** is PEO with 15 v/v% Er₂O₃ nanoparticles, **P.Er20** is PEO with 20 v/v% Er₂O₃ nanoparticles, and **P.Er25** is PEO with 25 v/v% Er₂O₃ nanoparticles..... 142

Figure 4.34 Crystalline phase and structure of PEO/Er₂O₃ nanofibres in Batch A. (a) **P.Er2** is a nanofibre formulation of PEO with 2 v/v% Er₂O₃ nanoparticles. (b) **P.Er4** is a nanofibre formulation of PEO with 4 v/v% Er₂O₃ nanoparticles. (c) **P.Er6** is a nanofibre formulation of PEO with 6 v/v% Er₂O₃ nanoparticles. (d) **P.Er8** is a nanofibre formulation of PEO with 8 v/v% Er₂O₃ nanoparticles..... 144

Figure 4.35 Crystalline phase and structure of PEO/Er₂O₃ nanofibres in Batch B. (a) **P.Er10** is a nanofibre formulation of PEO with 10 v/v% Er₂O₃ nanoparticles. (b) **P.Er15** is a nanofibre formulation of PEO with 15 v/v% Er₂O₃ nanoparticles. (c) **P.Er20** is a nanofibre formulation of PEO with 20 v/v% Er₂O₃ nanoparticles. (d) **P.Er25**

	is a nanofibre formulation of PEO with 25 v/v% Er ₂ O ₃ nanoparticles.....	147
Figure 4.36	Release profile of PEO/Er ₂ O ₃ nanofibres with different formulations in Batch A. (a) P.Er2 is a nanofibre formulation of PEO with 2 v/v% Er ₂ O ₃ nanoparticles. (b) P.Er4 is a nanofibre formulation of PEO with 4 v/v% Er ₂ O ₃ nanoparticles. (c) P.Er6 is a nanofibre formulation of PEO with 6 v/v% Er ₂ O ₃ nanoparticles. (d) P.Er8 is a nanofibre formulation of PEO with 8 v/v% Er ₂ O ₃ nanoparticles.....	150
Figure 4.37	Schematic illustration of the fibre release mechanism upon contact with the PBS contributes to the release rate profile.....	151
Figure 4.38	Release profile of PEO/Er ₂ O ₃ nanofibres with different formulations in Batch B. (a) P.Er10 is a nanofibre formulation of PEO with 10 v/v% Er ₂ O ₃ nanoparticles. (b) P.Er15 is a nanofibre formulation of PEO with 15 v/v% Er ₂ O ₃ nanoparticles. (c) P.Er20 is a nanofibre formulation of PEO with 20 v/v% Er ₂ O ₃ nanoparticles. (d) P.Er25 is a nanofibre formulation of PEO with 25 v/v% Er ₂ O ₃ nanoparticles.....	153
Figure 4.39	Dose-response curve of Er ₂ O ₃ nanoparticles and different formulations of PEO with low concentrations of Er ₂ O ₃ nanoparticles loading from 2% to 8% in breast cancer cell line (MCF-7): (a) Low dose concentrations from 10 µg/ml to 100 µg/ml and (b) High dose concentrations from 100 µg/ml to 1000 µg/ml. All experiments were performed in triplicate (n = 3). The asterisk (*) indicates a significant difference with $p < 0.05 - 0.01$, (**) indicates a significant difference with $p < 0.01 - 0.001$ and (***) indicates a significant difference with $p < 0.000$	156
Figure 4.40	Dose-response curve of Er ₂ O ₃ nanoparticles and different formulations of PEO with high concentrations of Er ₂ O ₃ nanoparticles loading from 10% to 25% in breast cancer cell line (MCF-7): (a) Low dose concentrations from 10 µg/ml to 100 µg/ml and (b) High dose concentrations from 100 µg/ml to 1000 µg/ml.	

	All experiments were performed in triplicate (n = 3). The asterisk (*) indicates a significant difference with $p < 0.05 - 0.01$, and (**) indicates a significant difference with $p < 0.01 - 0.001$	159
Figure 4.41	Number of colonies formed after 9 days of treatment for Batch A. All experiments were performed in triplicate (n = 3). The paired t-test of each formulation normalised to control (untreated cells) was performed in breast cancer (MCF-7) cells. The asterisk (*) indicates a significant difference with $p < 0.05 - 0.01$, and (**) indicates a significant difference with $p < 0.01 - 0.001$	163
Figure 4.42	Number of colonies formed after 9 days of treatment for Batch B. All experiments were performed in triplicate (n = 3). The paired t-test of each formulation normalised to control (untreated cells) was performed in breast cancer (MCF-7) cells. The asterisk (**) indicates a significant difference with $p < 0.01 - 0.001$, and (***) indicates a significant difference with $p < 0.000$	165
Figure 4.43	MCF-7 cell morphology exposed with a 10 $\mu\text{g/ml}$ dose of the P.Er4 formulation for 24 hours of treatment. (a) An inverted phase-contrast image of a semithin section of treated cells through toluidine blue staining. (b) The treated cell morphology observation under EFTEM. The orange circles highlight the autophagic vacuoles labelled A_v . Label N is the nucleus, and C is the cytoplasm. The yellow circles indicate the presence of Er_2O_3 nanoparticles.....	167
Figure 4.44	Inverted phase-contrast microscope images viewed at 200x magnification. (a) Control (untreated MCF-7 cells). (b) Treated MCF-7 cells with 10 $\mu\text{g/ml}$ dose of the P.Er4 formulation.	168
Figure 4.45	MCF-7 cell morphology exposed with a 10 $\mu\text{g/ml}$ dose of the P.Er10 formulation for 24 hours of treatment. (a) An inverted phase-contrast image of a semithin section of treated cells through toluidine blue staining. (b) The treated cell morphology observation under EFTEM. The purple circles highlight the autophagic vacuoles labelled A_v . Label N is the nucleus, and C is	

	the cytoplasm. The yellow circles indicate the presence of Er_2O_3 nanoparticles.....	170
Figure 4.46	Inverted phase-contrast microscope images at 200x magnification. (a) Control (untreated MCF-7 cells). (b) Treated MCF-7 cells in a 10 $\mu\text{g}/\text{ml}$ dose of the P.Er10 formulation.....	172
Figure 4.47	T1-weighted image signal intensities for all samples. (a) Agarose gel acts as a positive control, whereas Er_2O_3 nanoparticles act as a negative control. The nanofibre formulation for Batch A: (b) P.Er2 is PEO with 2 v/v% Er_2O_3 nanoparticles, (c) P.Er4 is PEO with 4 v/v% Er_2O_3 nanoparticles, (d) P.Er6 is PEO with 6 v/v% Er_2O_3 nanoparticles, and (e) P.Er8 is PEO with 8 v/v% Er_2O_3 nanoparticles. All experiments were performed in triplicate (n =3).	174
Figure 4.48	T1-weighted images for all samples at a 1000 $\mu\text{g}/\text{ml}$ dose concentration (except agarose gel). TE = 15 ms and TR = 4000 ms with a pixel size of 0.94 mm x 0.94 mm and signal-to-noise (SNR) of 102%.	175
Figure 4.49	Comparison of longitudinal relaxation time (T1) between Er_2O_3 nanoparticles (negative control) and PEO/ Er_2O_3 nanofibres in Batch A.	175
Figure 4.50	T2-weighted image signal intensities for all samples. (a) Agarose gel acts as a positive control, whereas Er_2O_3 nanoparticles act as a negative control. The nanofibre formulation for Batch A: (b) P.Er2 is PEO with 2 v/v% Er_2O_3 nanoparticles, (c) P.Er4 is PEO with 4 v/v% Er_2O_3 nanoparticles, (d) P.Er6 is PEO with 6 v/v% Er_2O_3 nanoparticles, and (e) P.Er8 is PEO with 8 v/v% Er_2O_3 nanoparticles. All experiments were performed in triplicate (n = 3).	177
Figure 4.51	T2-weighted images for all samples at a 1000 $\mu\text{g}/\text{ml}$ dose concentration (except agarose gel). TR = 2000 ms and TE = 100 ms with a pixel size of 0.94 mm x 0.94 mm and signal-to-noise (SNR) of 119%.	178

Figure 4.52	Comparison of transverse relaxation time (T2) between Er ₂ O ₃ nanoparticles (negative control) and PEO/Er ₂ O ₃ nanofibres in Batch A.	179
Figure 4.53	Comparative analysis of relaxivity values between Er ₂ O ₃ nanoparticles (negative control) and PEO/Er ₂ O ₃ nanofibres in Batch A. (a) Longitudinal relaxivity (r ₁). (b) Transverse relaxivity (r ₂).	181
Figure 4.54	T1-weighted image signal intensities for all samples. Agarose gel acts as a positive control. The nanofibre formulation for Batch B: (a) P.Er10 is PEO with 10 v/v% Er ₂ O ₃ nanoparticles, (b) P.Er15 is PEO with 15 v/v% Er ₂ O ₃ nanoparticles, (c) P.Er20 is PEO with 20 v/v% Er ₂ O ₃ nanoparticles, and (d) P.Er25 is PEO with 25 v/v% Er ₂ O ₃ nanoparticles. All experiments were performed in triplicate (n = 3).	184
Figure 4.55	T1-weighted images for all samples at a 1000 µg/ml dose concentration (except agarose gel). TE = 15 ms and TR = 4000 ms with a pixel size of 0.94 mm x 0.94 mm and signal-to-noise (SNR) of 102%.	185
Figure 4.56	Comparison of longitudinal relaxation time (T1) between Er ₂ O ₃ nanoparticles (negative control) and PEO/Er ₂ O ₃ nanofibres in Batch B.	186
Figure 4.57	T2-weighted image signal intensities for all samples. Agarose gel acts as a positive control. The nanofibre formulation for Batch B: (a) P.Er10 is PEO with 10 v/v% Er ₂ O ₃ nanoparticles, (b) P.Er15 is PEO with 15 v/v% Er ₂ O ₃ nanoparticles, (c) P.Er20 is PEO with 20 v/v% Er ₂ O ₃ nanoparticles, and (d) P.Er25 is PEO with 25 v/v% Er ₂ O ₃ nanoparticles. All experiments were performed in triplicate (n = 3).	188
Figure 4.58	T2-weighted images for all samples at a 1000 µg/ml dose concentration (except agarose gel). TR = 2000 ms and TE = 100 ms with a pixel size of 0.94 mm x 0.94 mm and signal-to-noise (SNR) of 119%.	189

Figure 4.59	Schematic illustration of the Brownian motion of nanoparticles in the agarose gel. As demonstrated, the movement of the nanoparticles is restricted due to nanofiller loading, thus contributing to higher molarity volume, resulting in darker images in the T2 signal.	189
Figure 4.60	Comparison of transverse relaxation time (T2) between Er ₂ O ₃ nanoparticles (negative control) and PEO/Er ₂ O ₃ nanofibres in Batch B.....	190
Figure 4.61	Comparative analysis of relaxivity values between Er ₂ O ₃ nanoparticles (negative control) and PEO/Er ₂ O ₃ nanofibres in Batch B. (a) Longitudinal relaxivity (r ₁). (b) Transverse relaxivity (r ₂).....	192
Figure 4.62	<i>In vitro</i> T1-weighted image signal intensities for all samples. (a) Untreated cells act as a positive control, whereas treated cells with Er ₂ O ₃ nanoparticles act as a negative control. MCF-7 cells were treated with the nanofibre formulation in Batch A: (b) P.Er2 is PEO with 2 v/v% Er ₂ O ₃ nanoparticles, (c) P.Er4 is PEO with 4 v/v% Er ₂ O ₃ nanoparticles, (d) P.Er6 is PEO with 6 v/v% Er ₂ O ₃ nanoparticles, and (e) P.Er8 is PEO with 8 v/v% Er ₂ O ₃ nanoparticles. All experiments were performed in triplicate (n = 3).	198
Figure 4.63	<i>In vitro</i> T1-weighted images for all samples at a 1000 µg/ml dose concentration (except untreated cells). TE = 15 ms and TR = 4000 ms with a pixel size of 0.94 mm x 0.94 mm and signal-to-noise (SNR) of 102%.	199
Figure 4.64	Comparison of <i>in vitro</i> longitudinal relaxation time (T1) between Er ₂ O ₃ nanoparticles (negative control) and PEO/Er ₂ O ₃ nanofibres in Batch A.....	200
Figure 4.65	<i>In vitro</i> T2-weighted image signal intensities for all samples. (a) Untreated cells act as a positive control, whereas treated cells with Er ₂ O ₃ nanoparticles act as a negative control. MCF-7 cells were treated with the nanofibre formulation in Batch A: (b) P.Er2 is	

	PEO with 2 v/v% Er ₂ O ₃ nanoparticles, (c) P.Er4 is PEO with 4 v/v% Er ₂ O ₃ nanoparticles, (d) P.Er6 is PEO with 6 v/v% Er ₂ O ₃ nanoparticles, and (e) P.Er8 is PEO with 8 v/v% Er ₂ O ₃ nanoparticles. All experiments were performed in triplicate (n = 3).	202
Figure 4.66	<i>In vitro</i> T2-weighted images for all samples at a 1000 µg/ml dose concentration (except untreated cells). TR = 2000 ms and TE = 100 ms with a pixel size of 0.94 mm x 0.94 mm and signal-to-noise (SNR) of 119%.	203
Figure 4.67	Comparison between <i>in vitro</i> transverse relaxation time (T2) for Er ₂ O ₃ nanoparticles (negative control) and PEO/Er ₂ O ₃ nanofibres in Batch A.....	204
Figure 4.68	Comparative analysis of <i>in vitro</i> relaxivity values between Er ₂ O ₃ nanoparticles (negative control) and PEO/Er ₂ O ₃ nanofibres in Batch A. (a) <i>In vitro</i> longitudinal relaxivity (r ₁). (b) <i>In vitro</i> transverse relaxivity (r ₂).	206
Figure 4.69	<i>In vitro</i> T1-weighted image signal intensities for all samples. Untreated cells act as a positive control. MCF-7 cells were treated with the nanofibre formulation in Batch B: (a) P.Er10 is PEO with 10 v/v% Er ₂ O ₃ nanoparticles, (b) P.Er15 is PEO with 15 v/v% Er ₂ O ₃ nanoparticles, (c) P.Er20 is PEO with 20 v/v% Er ₂ O ₃ nanoparticles, and (d) P.Er25 is PEO with 25 v/v% Er ₂ O ₃ nanoparticles. All experiments were performed in triplicate (n = 3).	209
Figure 4.70	<i>In vitro</i> T1-weighted images for all samples at a 1000 µg/ml dose concentration (except untreated cells). TE = 15 ms and TR = 4000 ms with a pixel size of 0.94 mm x 0.94 mm and signal-to-noise (SNR) of 102%.	210
Figure 4.71	Comparison of <i>in vitro</i> longitudinal relaxation time (T1) between Er ₂ O ₃ nanoparticles (negative control) and PEO/Er ₂ O ₃ nanofibres in Batch B.....	211

Figure 4.72	<i>In vitro</i> T2-weighted image signal intensities for all samples. Untreated cells act as a positive control. MCF-7 cells were treated with the nanofibre formulation in Batch B: (a) P.Er10 is PEO with 10 v/v% Er ₂ O ₃ nanoparticles, (b) P.Er15 is PEO with 15 v/v% Er ₂ O ₃ nanoparticles, (c) P.Er20 is PEO with 20 v/v% Er ₂ O ₃ nanoparticles, and (d) P.Er25 is PEO with 25 v/v% Er ₂ O ₃ nanoparticles. All experiments were performed in triplicate (n = 3).	212
Figure 4.73	<i>In vitro</i> T2-weighted images for all samples at a 1000 µg/ml dose concentration (except untreated cells). TR = 2000 ms and TE = 100 ms with a pixel size of 0.94 mm x 0.94 mm and signal-to-noise (SNR) of 119%.	214
Figure 4.74	Comparison of <i>in vitro</i> transverse relaxation time (T2) between Er ₂ O ₃ nanoparticles (negative control) and PEO/Er ₂ O ₃ nanofibres in Batch B.....	214
Figure 4.75	Comparative analysis of <i>in vitro</i> relaxivity values between Er ₂ O ₃ nanoparticles (negative control) and PEO/Er ₂ O ₃ nanofibres in Batch B. (a) <i>In vitro</i> longitudinal relaxivity (r ₁). (b) <i>In vitro</i> transverse relaxivity (r ₂).	216
Figure 4.76	<i>In vitro</i> T1- and T2-weighted image signal intensities for 10 µg/ml dose of the P.Er4 formulation. Untreated cells act as a positive control. MCF-7 cells were treated with a 10 µg/ml dose of the P.Er4 formulation for 24 hours. The nanofibre formulation of the P.Er4 is PEO with 4 v/v% Er ₂ O ₃ nanoparticles. All experiments were performed in triplicate (n = 3). The asterisk (**) indicates a significant difference with p < 0.01 – 0.001, and (***) indicates a significant difference with p < 0.000.	222
Figure 4.77	Comparisons of <i>in vitro</i> T1 and T2-weighted image signal intensities between untreated cells (positive control) and treated cells with 10 µg/ml dose of the P.Er4 formulation. The nanofibre formulation of the P.Er4 is PEO with 4 v/v% Er ₂ O ₃ nanoparticles. (a) <i>In vitro</i> T1-weighted images at TE = 15 ms, TR = 250 ms to	

4000 ms with a pixel size of 0.94 mm x 0.94 mm and signal-to-noise (SNR) of 102%. (b) *In vitro* T2-weighted images at TR = 2000 ms, TE = 10 ms to 100 ms with a pixel size of 0.94 mm x 0.94 mm and SNR of 119%. 223

LIST OF SYMBOLS

g	gravitational
δ	scissor/deformation
v	stretch
ρ	rock
τ	twist
ω	wag
$\&$	and

LIST OF ABBREVIATIONS

1D	One-dimensional
^1H	Hydrogen proton
2D	Two-dimensional
3D	Three-dimensional
AFM	Atomic force microscopy
AMDI	Advanced Medical and Dental Institute
ANOVA	Analysis of variance
ATP	Adenosine triphosphate
Au	Gold
B_0	External magnetic field
BSE	Back-scattered electron
Ca^{2+}	Calcium ion
C_{DA}	Analytical concentration of contrast ion
CH_2	Methylene
CI	Crystallinity index
CO_2	Carbon dioxide
CT	Computed tomography
DMEM	Dulbecco's Modified Eagle's Medium
DMSO	Dimethyl sulfoxide
DNA	Deoxyribonucleic acid
DOX	Doxorubicin hydrochloride
Dy_2O_3	Dysprosium oxide
e.g.	Example given
EDTA	Ethylenediaminetetraacetic acid
EDX	Energy-dispersive X-ray
EFTEM	Energy-filtered transmission electron microscopy
EMA	European Medicines Agency
EMEM	Eagle's minimum essential medium
Er	Erbium
ER+	Estrogen-positive
Er_2O_3	Erbium oxide

ES	Electrospinning
FBS	Fetal bovine serum
FDA	Food and Drug Administration
Fe ₂ O ₃	Ferric oxide
FOV	Field of view
FTIR	Fourier transform infrared resonance
GBCA	Gadolinium-based contrast agent
Gd	Gadolinium
Gd(OH) ₃	Gadolinium(III) hydroxide
Gd-DTPA	Gd-diethylenetriaminepentaacetate or Magnevist
HeLa	Human cervical cancer cells
Hep-G2	Human hepatocellular carcinoma
HR-	Hormone receptor-negative
HR+	Hormone receptor-positive
HRTEM	High-resolution transmission electron microscopy
HSF	Human skin fibroblast
ICP-OES	Inductively coupled plasma-optical emission spectroscopy
M ₀	Maximum magnetisation at full recovery along the z-axis
MCF-7	Michigan Cancer Foundation-7
MDA-MB-231	Triple-negative breast cancer cell line
MG-63	Osteoblast cell line
Mn	Manganese
MRI	Magnetic resonance imaging
MTS	3-(4,5-dimethylthiazol-2-yl)-5-(3-carboxymethoxyphenyl)-2-(4-sulfophenyl)-2H-tetrazolium)
M _z	Net magnetisation vector at the z-axis
NaHCO ₃	Sodium bicarbonate
NaOH	Sodium hydroxide
NEX	Number of excitation
Ni	Nickel
NIPS	Non-solvent-induced phase separation
NIR	Near-infrared region
NPs	Nanoparticles
NSF	Nephrogenic systemic fibrosis
P.Er10	Nanofibre formulation of PEO with 10 v/v% Er ₂ O ₃ nanoparticles

P.Er15	Nanofibre formulation of PEO with 15 v/v% Er ₂ O ₃ nanoparticles
P.Er2	Nanofibre formulation of PEO with 2 v/v% Er ₂ O ₃ nanoparticles
P.Er20	Nanofibre formulation of PEO with 20 v/v% Er ₂ O ₃ nanoparticles
P.Er25	Nanofibre formulation of PEO with 25 v/v% Er ₂ O ₃ nanoparticles
P.Er4	Nanofibre formulation of PEO with 4 v/v% Er ₂ O ₃ nanoparticles
P.Er6	Nanofibre formulation of PEO with 6 v/v% Er ₂ O ₃ nanoparticles
P.Er8	Nanofibre formulation of PEO with 8 v/v% Er ₂ O ₃ nanoparticles
P4	Nanofibre formulation of 4 wt% PEO
P5	Nanofibre formulation of 5 wt% PEO
P6	Nanofibre formulation of 6 wt% PEO
P7	Nanofibre formulation of 7 wt% PEO
P8	Nanofibre formulation of 8 wt% PEO
PBS	Phosphate-buffered saline
PCL	Poly (ϵ -caprolactone)
PCU	polycarbonate-urethanes
PEG	Poly (ethylene) glycol
Pen-strep	Penicillin-streptomycin
PEO	Poly (ethylene) oxide
PES	Polyethersulfone
PET	Positron emission tomography
PET	Poly (ethylene) terephthalate
PGA	Polyglycolic acid
PGLu	Polyglutamic acid
pH	Potential of hydrogen
PHA	Polyalkenoate
PLA	Polylactic acid
PLGA	Poly (lactic-co-glycolic acid)
PPM	Part per million
PR+	Progesterone-positive
PVP	Polyvinyl pyrrolidone
R1	Longitudinal or spin-lattice relaxation rate
r ₁	Longitudinal or spin-lattice relaxivity
R2	Transverse or spin-spin relaxation rate
r ₂	Transverse or spin-spin relaxivity

R _a	Average surface roughness
RES	Reticuloendothelial
RF	Radiofrequency
RH	Relative humidity
ROI	Region of interest
ROS	Reactive oxygen species
RPMI-1640	Roswell Park Memorial Institute-1640
SD	Standard deviation
SDS	Sodium dodecyl sulfate
SE	Secondary electron
SI	Signal intensity
SNR	Signal-to-noise ratio
SPECT	Single-photon emission computerised tomography
SPION	Superparamagnetic iron oxide
T1	Longitudinal or spin-lattice relaxation time
T2	Transverse or spin-spin relaxation time
T25	25 cm ² culture flask
T75	75 cm ² culture flask
T _c	Crystallisation temperature
TE	Echo time
TIPS	Thermally-induced phase separation
T _m	Melting point temperature
TR	Repetition time
Tukey HSD	Tukey's honestly significant difference
UV-Vis	Ultraviolet-visible
V _c	Critical voltage
VIPS	Vapour-induced phase separation
vs	versus
WHO	World Health Organisation
ZAWAIN	Zakat Universiti Sains Malaysia

LIST OF APPENDICES

Appendix A	List of chemical compounds
Appendix B	List of apparatus
Appendix C	List of equipment
Appendix D	Percentage of cell viability after 24 hours of treatment with PEO nanofibres
Appendix E	Percentage of cell viability after 24 hours of treatment with Er ₂ O ₃ nanoparticles and PEO/Er ₂ O ₃ nanofibres
Appendix F	T1-weighted image signal intensities at TE = 15 ms and TR = 250 ms to 4000 ms with different dose concentrations for all samples
Appendix G	T2-weighted image signal intensities at TR = 2000 ms and TE = 10 ms to 100 ms with different dose concentrations for all samples
Appendix H	Longitudinal relaxation rate (1/T1) and relaxation time (T1) based on T1-weighted image signal intensities with different dose concentrations for all samples
Appendix I	Transverse relaxation rate (1/T2) and relaxation time (T2) based on T2-weighted image signal intensities with different dose concentrations for all samples
Appendix J	<i>In vitro</i> T1-weighted image signal intensities at TE = 15 ms and TR = 250 ms to 4000 ms with different dose concentrations for all samples
Appendix K	<i>In vitro</i> T2-weighted image signal intensities at TR = 2000 ms and TE = 10 ms to 100 ms with different dose concentrations for all samples
Appendix L	<i>In vitro</i> longitudinal relaxation rate (1/T1) and <i>in vitro</i> relaxation time (T1) based on <i>in vitro</i> T1-weighted image signal intensities with different dose concentrations for all samples
Appendix M	<i>In vitro</i> transverse relaxation rate (1/T2) and <i>in vitro</i> relaxation time (T2) based on <i>in vitro</i> T2-weighted image signal intensities with different dose concentrations for all samples

**SINTESIS DAN PENILAIAN POLI (ETELINA) OKSIDA/ERBIUM
OKSIDA BERPOTENSI SEBAGAI DIAGNOSTIK NANOSERAT UNTUK
PENGIMEJAN MAGNETIK RESONAN**

ABSTRAK

Kemajuan dalam nanoteknologi telah membawa kepada pembangunan bahan berskala nano dalam aplikasi diagnostik yang berpotensi tinggi untuk meningkatkan nilai diagnosis kanser yang mungkin memberi kesan ketara kepada penjagaan kesihatan pada masa hadapan. Agen diagnostik untuk pengimejan magnetik resonan (MRI) telah dibangunkan dalam kajian ini dengan menggunakan kaedah pemintalan elektro untuk membenamkan nanozarah erbium oksida (Er_2O_3) ke dalam matriks poli (etelina) oksida (PEO). Tambahan pula, ciri-ciri nanoserat PEO dan PEO/ Er_2O_3 telah disahkan menggunakan FESEM-EDX, AFM, FTIR, UV-Vis, Zetasizer, HRTEM, XRD, dan ICP-OES. Kajian sitotoksik “*in vitro*” dan pembentukan koloni telah dijalankan ke atas sel MCF-7 untuk menyiasat kesan formulasi nanoserat PEO and PEO/ Er_2O_3 terhadap ciri-ciri perkembangan kanser. Dapatan menunjukkan bahawa formulasi campuran polimer dengan dan tanpa pengisinano telah mempengaruhi diameter, ketebalan, dan kekasaran permukaan serat. Penemuan juga mendedahkan bahawa nanoserat PEO mempamerkan ciri-ciri bukan sitotoksik terhadap sel MCF-7. Nanoserat 5 wt% PEO (P5) telah dicadangkan sebagai formulasi nanoserat optimum yang sesuai sebagai matriks polimer atau pembawa untuk tujuan diagnostik. Penyiasatan lanjut sitotoksik nanoserat PEO/ Er_2O_3 menunjukkan percambahan sel terhadap pemuatan pengisinano bagi kepekatan dos rendah daripada 0 – 100 $\mu\text{g/ml}$, manakala daya maju sel menurun telah diperhatikan bagi kepekatan dos tinggi daripada 100 – 1000 $\mu\text{g/ml}$. Namun begitu, tiada formulasi menghalang 50% daya

maju sel. Hasil dapatan mencadangkan formulasi nanoserat PEO dengan 2 v/v% nanozarah Er_2O_3 (P.Er2) adalah ideal untuk tujuan diagnostik berikutan ciri-ciri bukan sitotoksik. Sebaliknya, formulasi nanoserat PEO dengan 4 v/v% nanozarah Er_2O_3 (P.Er4) mempunyai kesan dwi yang berguna bagi kedua-dua tujuan diagnostik dan terapeutik. Pengambilan selular menunjukkan bahawa nanozarah telah diserap oleh sel-sel melalui endositosis tanpa mengakibatkan kerosakan struktur kepada membran selular. MRI “*in vitro*” menunjukkan bahawa nanoserat PEO/ Er_2O_3 boleh berfungsi sebagai T2 dan T1-T2 dwi-mod diagnostik nanoserat, sekaligus menggandakan sensitiviti pengesanan untuk diagnosis kanser. Formulasi nanoserat PEO dengan 4 v/v% nanozarah Er_2O_3 (P.Er4) telah dicadangkan sebagai formulasi nanoserat yang ideal untuk T1-T2 dwi-mod diagnostik nanoserat MRI. Kajian ini menunjukkan bahawa dengan menetapkan masa gema (TE) 15 ms, kesan kontras optimum untuk imej berwajaran-T1 “*in vitro*” telah ditentukan berada dalam masa pengulangan (TR) yang boleh dilaraskan dari 250 ms hingga 4000 ms. Sebaliknya, untuk imej berwajaran-T2 “*in vitro*”, dengan menetapkan TR 2000 ms, kesan kontras optimum telah didapati berada dalam TE yang boleh dilaraskan dari 10 ms hingga 60 ms. Kesimpulannya, nanoserat PEO/ Er_2O_3 menunjukkan keupayaan yang menjanjikan dalam meningkatkan sensitiviti pengesanan diagnosis kanser, menjadikannya sebagai agen diagnostik yang bernilai untuk MRI.

**SYNTHESIS AND EVALUATION OF POLY (ETHYLENE)
OXIDE/ERBIUM OXIDE AS POTENTIAL DIAGNOSTIC NANOFIBRES
FOR MAGNETIC RESONANCE IMAGING**

ABSTRACT

Advances in nanotechnology have led to the development of nanoscale materials for diagnostic applications, with a high potential to improve cancer diagnosis value, significantly impacting the future of healthcare. A diagnostic agent for magnetic resonance imaging (MRI) was developed in the current study using the electrospinning method to embed erbium oxide (Er_2O_3) nanoparticles in a poly (ethylene) oxide (PEO) matrix. Moreover, the characteristics of PEO and PEO/ Er_2O_3 nanofibres were confirmed using FESEM-EDX, AFM, FTIR, UV-Vis, Zetasizer, HRTEM, XRD, and ICP-OES. *In vitro* cell cytotoxicity and colony formation studies were conducted on MCF-7 cells to investigate the effects of PEO and PEO/ Er_2O_3 nanofibre formulations on cancer progression characteristics. Findings demonstrated that the polymer blend formulations with and without nanofiller affected fibre diameter, thickness, and surface roughness. Findings also revealed that PEO nanofibres exhibited non-cytotoxic characteristics towards MCF-7 cells. The 5 wt% PEO nanofibre (P5) was recommended as the optimal nanofibre formulation suitable as a polymer matrix or carrier for diagnostic purposes. Further cytotoxicity investigation of PEO/ Er_2O_3 nanofibres demonstrated cell proliferation over nanofiller loading for low dose concentration from 0 – 100 $\mu\text{g}/\text{ml}$, whereas a reduction in cell viability was observed for high dose concentration from 100 – 1000 $\mu\text{g}/\text{ml}$. Nevertheless, none of the formulations inhibited 50% of the cell viability. Findings recommended that the nanofibre formulation of PEO with 2 v/v% Er_2O_3 nanoparticles (P.Er2) was ideal for

diagnostic purposes due to its non-cytotoxic characteristics. In contrast, the nanofibre formulation of PEO with 4 v/v% Er₂O₃ nanoparticles (P.Er4) had a dual effect, useful for both diagnostic and therapeutic purposes. The cellular uptake indicated that nanoparticles were internalised by the cells *via* endocytosis without inducing structural damage to the cellular membrane. The *in vitro* MRI demonstrated that PEO/Er₂O₃ nanofibres could serve as T2 and T1-T2 dual-mode diagnostic nanofibres, thus doubling the detection sensitivity for cancer diagnosis. The nanofibre formulation of PEO with 4 v/v% Er₂O₃ nanoparticles (P.Er4) was recommended as the ideal formulation for a T1-T2 dual-mode MRI diagnostic nanofibre. The study revealed that upon setting an echo time (TE) of 15 ms, the optimal contrast effect for *in vitro* T1-weighted images was determined to be within a tunable repetition time (TR) from 250 ms to 4000 ms. Conversely, for *in vitro* T2-weighted images, upon setting a TR of 2000 ms, the optimal contrast effect was found to be within a tunable TE range of 10 ms to 60 ms. In conclusion, PEO/Er₂O₃ nanofibres exhibited a promising capability of enhancing the sensitivity of cancer diagnosis detection, positioning them as valuable diagnostic agents for MRI.

CHAPTER 1

INTRODUCTION

1.1 Background of the study

Medical imaging modalities are powerful tools for visualising the abnormal tissue or tumour at the target site of the related disease. They are a fundamental approach to diagnosing and detecting the tumour's early stage or locating its origin inside the human body. Examples of medical imaging modalities are magnetic resonance imaging (MRI), nuclear magnetic resonance (NMR), fluorescence, ultrasound, computed tomography (CT) scan, and mammography. These technologies become necessary in the medical field to thoroughly examine the patient's internal body condition and follow up on tumour regression.

MRI is a non-invasive medical imaging modality and clinically validated technique that has offered a high spatial and temporal resolution for the structural and functional examination of soft tissue without harmful radiation since the 1980s. It uses a strong magnetic field of around 1.5 to 3.0 Tesla and differs from a CT scan and X-rays as it does not emit harmful ionising radiation. MRI scanner is a giant doughnut-shaped component surrounded by an enormous circular magnet with a strong magnetic field, magnetic field gradient, and radio waves to generate the image of organ structures in the human body. However, due to its low sensitivity compared to other medical imaging modalities (e.g., positron emission tomography (PET) and single-photon emission computerised tomography (SPECT)), it needs a diagnostic agent (also known as a contrast agent) to enhance the signal contrast and improve image resolution.

Diagnostic agents for MRI are typically administered directly by mouth or indirectly through intravenous injection into the bloodstream before an MRI

examination. These agents rely on paramagnetic metal ions and are assessed based on their relaxivity, which refers to the increased rate of relaxation of water protons in a concentration-dependent manner measurable under an MRI scan. Diagnostic agents are classified into two primary types: positive (T1) diagnostic agents and negative (T2) diagnostic agents. T1 diagnostic agents shorten the longitudinal relaxation times of protons, producing brighter signal intensities on MRI images. In comparison, transverse relaxation times of protons are shortened by T2 diagnostic agents, resulting in darker signals in MRI images. The differing effects on relaxation times allow the two types of diagnostic agents to enhance MRI contrast in complementary ways.

Gadolinium-based diagnostic agents (GBCAs) are clinically preferable as T1 diagnostic agents. These agents exhibit a remarkable capacity to enhance the quality of MRI images by diminishing the T1 relaxation time, resulting in higher-resolution images of the desired anatomy. However, these agents are constrained by their notably suboptimal T1 relaxation efficiency and rapid renal clearance with elimination half-life ranges between 1 to 2 hours (Falk Delgado et al., 2019; Gale and Caravan, 2018; Yang et al., 2021). Furthermore, Gd³⁺ ion retention in the body exhibited adverse effects in patients with advanced kidney disease, which could cause nephrogenic systemic fibrosis (NSF). Gd is also retained throughout the body, including the brain, in patients with normal renal function, and the presence of Gd can persist months to years after the last administration of a GBCA (Hojreh et al., 2020; Layne et al., 2018; Le Fur and Caravan, 2019). Therefore, some linear GBCAs were withdrawn from the market or restricted from use by the European Medicines Agency (EMA) in 2017 (Falk Delgado et al., 2019).

On the other hand, T2 diagnostic agents are usually superparamagnetic nanoparticles and ferromagnetic nanoparticles. Among established T2 diagnostic

agents, superparamagnetic iron oxide nanoparticles (SPIONs) have raised much interest in the scientific community for their potential use in diagnostic purposes, especially in MRI. SPIONs have emerged as a favourable alternative to GBCAs for viewing primary or metastatic liver cancers, as they pose less risk to patients with renal conditions (Lee et al., 2022). Despite having large saturation magnetisation that assists in distinguishing between normal and abnormal tissues and having a long half-life, these effects resulted in signal reduction that consequently leads to the image darkening and poor resolution, and artefacts are generated when disturbed by high magnetic field inhomogeneity and sensitivity effects. Therefore, it makes the sensitivity for pathological diagnosis slightly poor (Dulińska-Litewka et al., 2019; Kim et al., 2016; Polu and Rhee, 2016).

Cancer ranks globally as the second leading cause of mortality. Breast cancer, in particular, exerts a significant mortality impact, with less than 30% of patients surviving beyond five years, according to statistics (Arnold et al., 2022; Riggio et al., 2021). Every 1 in 19 individuals is at risk of breast cancer, with more than 50% among women aged 21 to 30 (CodeBluesiti, 2022; Lee et al., 2019). Breast cancer represents one of the most prevalent malignancies afflicting women in Malaysia. According to the latest World Health Organisation (WHO) data published in 2020, breast cancer deaths in Malaysia reached 3503 or 11.9% of total deaths for all cancers among women (World Health Organization, 2021). Detecting breast cancer poses challenges due to its low prognosis; by the time it is identified, it often reaches advanced stages, specifically stages 3 and 4, making effective intervention challenging (Azizah et al., 2019; Htay et al., 2021; Mahmud and Aljunid, 2018). Many risk factors can contribute to breast cancer (e.g., family history, alcohol consumption, smoking, lactation failure, environmental toxicants, unbalanced diet, and obesity) that should not be taken lightly.

Lack of awareness, inappropriate screening planning, delayed diagnosis and insufficient medical facilities are also the main reasons for the breast cancer mortality rate (Jahan et al., 2016; Kashyap et al., 2022; Mamun and Sabantina, 2023; Martins et al., 2020).

Breast cancer comprises four central subtypes: estrogen receptor-positive (ER+), hormone receptor-positive (HR+), progesterone receptor-positive (PR+), and hormone receptor-negative (HR-) or triple-negative disease. A key cell line used in in vitro breast cancer studies is MCF-7, derived in 1970 from a 69-year-old Caucasian woman. MCF-7 expresses ER+, PR+ and glucocorticoid receptors (Chekhun et al., 2013; Davidson et al., 2015). Despite similar clinical-pathological factors, breast cancer patients often respond differently to treatments and experience varied outcomes, reflecting the heterogeneity of molecular subtypes (Adinew et al., 2022). Despite that, several treatments are available for breast cancer, including chemotherapy, radiotherapy, phototherapy, surgery, hyperthermia therapy and immunotherapy (Jahan et al., 2016; Kashyap et al., 2022; Mamun and Sabantina, 2023; Martins et al., 2020).

Nanotechnology developments have fostered growing research interest in the unique properties of nanoscale materials. Nanoparticles (NPs) offer substantial potential as diagnostic agents to improve cancer diagnosis through excellent biocompatibility, selective tumour accumulation, reduced toxicity compared to conventional agents, and biological inertness. Designing highly sensitive paramagnetic NPs centres on three key criteria per Solomon-Bloembergen-Morgan theory: slow molecular rotation of the agent, optimal metal binding lifetimes, and unstable water molecule coordination to the metal centre (Westlund, 1995). For medical use, 10 nm to 50 nm NPs are preferred as this size range minimises the

formation of single magnetic domains through magnetic energy effects (Naseri et al., 2018; Sudakaran et al., 2017).

Based on frontier research, polymeric applications mainly focus on nanomedicine using electrospinning (ES) (Abid et al., 2019). It is simple, convenient, and cost-effective that utilises electrostatic forces to fabricate polymeric nanofibres. It is a promising approach with outstanding features such as high surface area to volume ratio, excellent mechanical properties, ease of functionalisation, tuneable surface morphology, and simplicity of production with large-scale productions. Due to these advantages, it encourages researchers to continuously innovate and design new products using this method to meet market demands that are more challenging each year. ES offers massive benefits in various applications, such as tissue engineering, drug delivery, wound dressing, magnetic hyperthermia, and diagnostic agent in imaging techniques (Bahnson et al., 2016; Bellat et al., 2016; Contardi et al., 2017; Isik et al., 2019; Ganesh et al., 2016; Irani et al., 2017; Liu et al., 2018; Lock et al., 2017; Morgan et al., 2016; Pérez-Nava et al., 2018; Tamm et al., 2016; Wang et al., 2016; Zhang et al., 2017). For example, polymeric nanofibres can simultaneously improve biodistribution and diagnosis of tumour sites in targeted drug delivery. Consequently, the encapsulation of the diagnostic agent into the polymeric nanofibre (which acts as a carrier) can be implemented in medical imaging.

1.2 Problem statement

Magnetic resonance imaging (MRI) is an excellent medical modality useful for soft tissue examination. However, the low sensitivity of the technique poses a challenge to achieving an accurate image of function at the molecular level. Therefore, a diagnostic agent is developed to overcome this problem, particularly Gadolinium-

based diagnostic agents for T1-weighted images or superparamagnetic iron oxide nanoparticle-based diagnostic agents for T2-weighted images. Although the development of diagnostic agents has achieved great success, single-mode diagnostic agents have unique advantages and limitations. For example, a single-mode (T1 or T2) diagnostic agent suffers from false-positive signals ubiquitously observed in tissues for each imaging mode acquisition. It is difficult to distinguish water and fat using single-mode diagnostic agents. However, with T1-T2 dual-mode imaging, these issues can be addressed. Water presents a low signal on T1-weighted images and a high signal on T2-weighted images. Fat presents a high signal on both T1- and T2-weighted images. Thus, it is easy to recognise water and fat with dual-mode imaging (Alipour et al., 2018).

The development of T1-T2 dual-mode diagnostic agents has emerged and attracted considerable attention since 2015 as a single platform to reduce uncertainties in MRI analysis, validate the reconstruction and visualisation of the data more accurately and reliably and acquire complementary and self-confirmed information to permit meaningful interpretation (Chen et al., 2022; Chen et al., 2016). The advantage of T1-T2 dual-mode diagnostic agents is that two diagnostic agents complement and emphasise each other strength; thus, accurately matching two weighted images in time and space eliminates pseudo signals and provides a higher-resolution imaging effect due to T1- and T2-weighted images can be obtained for the same tumour site under the same metabolic conditions (Cao et al., 2021; Wang et al., 2021).

Various types of T1-T2 dual-mode diagnostic agents have been reported so far. Among them, researchers are gaining interest in the combination of a T1 diagnostic agent (e.g., Gadolinium (Gd)) with a T2 diagnostic agent (e.g., superparamagnetic iron oxide nanoparticle (SPION)) or with other elements (e.g., dysprosium oxide (Dy_2O_3),

manganese (Mn)) (Cao et al., 2021; Keasberry et al., 2015; Li et al., 2016; Lu et al., 2022; Tegafaw et al., 2015). In this case, intense proton relaxation interference between the two different diagnostic agents, which attenuates the T1 contrast effect by the strong local magnetic field of the T2 diagnostic agent, is inevitable when they are in proximity (Kim et al., 2016).

Since Gd-based diagnostic agents (GBCAs) have a risk of causing nephrogenic systematic fibrosis (NSF) and SPION-based diagnostic agents exhibited large r_2/r_1 ratio causing poor T1 contrast, these factors were in concern to be considered as T1-T2 dual-mode diagnostic agent (Deka et al., 2019). Therefore, this research is defined as studying other paramagnetic elements for producing potential T1-T2 diagnostic agents in medical imaging modalities, especially MRI. In line with Gd in the periodic table, erbium (Er) has gained interest from researchers for its magnetic properties. However, its potential use as diagnostic nanofibres has not been studied yet. Selecting elements in the lanthanide (rare earth metal), the group gives considerable advantages in developing new diagnostic agents because of the possession of powerful paramagnetic properties and high density.

Er has a higher atomic number, mass, and density than Gd, which are 68, 167 u and 9.2 g/cm^3 , respectively. Er, with two unpaired electrons, is considered less toxic than Gd, which has seven unpaired electrons. It also has lower toxicity than lead and its compound (Liu et al., 2014). It possesses partially filled inner shells of electrons (4F and 5D subshells), excellent upconversion luminescent characteristics, stable paramagnetic properties, excellent photostability, long Stokes shift, and strong absorption and emission peaks. It also provides an extended lifetime, low phototoxicity to biological tissues, bioinert and non-interference with tissue autofluorescence (Rajaji et al., 2019; Reddy et al., 2017).

Various end-products have been incorporated with nanoscale materials that significantly improve the existing products or impart new functionalities to the related products based on their physicochemical properties. However, the wide applications of nanomaterials have raised health concerns regarding the potential toxicity of nanoparticles to humans. Their physical and chemical characteristics determine the toxicity of nanoparticles, including their shape, size, surface charge, stability, and chemical compositions of the core and shell (Bahadar et al., 2016; Brohi et al., 2017; Buchman et al., 2019; Huang et al., 2017; Sukhanova et al., 2018). Some nanoparticles are clinically approved for diagnostic applications (Anselmo and Mitragotri, 2019). Therefore, a study of the toxicity of nanoparticles is a must in nanoscale material research.

Electrospinning (ES) is an established technique to generate a unique morphology of one-dimensional (1D) nanostructure fibres to act as a matrix or carrier for encapsulating nanoparticles. It has been well-received as an effective method in producing fibres from nano to micro diameters for various applications. Therefore, selecting suitable polymers is crucial for this technique to suit its functionality for potential uses in diagnostics. These polymers can be either natural or synthetic with characteristics of biocompatible, non-toxic to induce a minor inflammatory response, bioinert, and biodegradable. Furthermore, the conjugation of a polymer as a coating material for diagnostic agents reduces toxicity and prolongs circulation time in blood vessels, which is suitable for diagnosis purposes (Yang et al., 2021). A polymer coating can also perform as a T1 diagnostic agent in MRI, thus beneficial in this study (Zhu et al., 2016).

Poly (ethylene) oxide (PEO) was used in this research due to its water-soluble, non-ionic, and highly hydrophilic properties. Moreover, it is certified by the Food and

Drug Administration (FDA) as a biocompatible, biodegradable, bioinert, and non-toxic polymer. Furthermore, it has shown high versatility as a carrier polymer. PEO dissolves in water and different organic solvents, giving it an extra suitability score in medical applications (Carrasco-Torres et al., 2019). It is preferable in various industrial applications, especially in the biomedical field, such as bone tissue engineering, drug delivery, green composite, wound dressing, and many more (Elsadek et al., 2022; Guo et al., 2022; Harish et al., 2022; Hong, 2016; Khandaker et al., 2022; Khunová et al., 2022; Li et al., 2022; Singh et al., 2020; Wu et al., 2018; Yuan et al., 2016). It can also be a stabilising and thickening agent (Hurtado et al., 2020). Furthermore, it is recognised in medical implantation for cranial and facial reconstruction (Paxton et al., 2019).

This study seeks to overcome the limitations of single-mode (T1 or T2) diagnostic agents, which often exhibit false-positive signals and difficulty distinguishing water and fat ubiquitously observed in tissues, by developing a T1-T2 dual-mode diagnostic agent using Er₂O₃ nanoparticles embedded into the PEO matrix using the electrospinning method.

1.3 Objectives of the study

The main objective of this research was to investigate a permissible concentration of PEO nanofibre formulation as a polymer matrix or carrier with potential use for diagnostic purposes. Next, PEO/Er₂O₃ nanofibres were synthesised and evaluated to find the ideal nanofibre formulation as a T1-T2 dual-mode MRI diagnostic agent. Several specific objectives were performed to accomplish the main objective, such as:

- a) To synthesise and characterise PEO and PEO/Er₂O₃ nanofibres based on their morphological structures, nanoparticle loading, and stability.
- b) To determine the cytotoxicity of PEO and PEO/Er₂O₃ nanofibres in a breast cancer cell line (MCF-7) with cell proliferation assay.
- c) To assess functional roles of PEO/Er₂O₃ nanofibres by colony formation assay and nanoparticle uptake analysis.
- d) To determine the resonance parameterisation of PEO/Er₂O₃ nanofibres in a breast cancer cell line (MCF-7) using MRI.

1.4 Scope of the study

This research is divided into three parts as follows:

Part 1 initiates the preliminary study and optimisation process in this research. It involved synthesising and characterising different formulations (wt%) of PEO nanofibres. The functional effects of PEO nanofibres were carried out using the MTS assay and colony formation assay in a breast cancer cell line (MCF-7). The optimal PEO nanofibre formulation with potential use as a polymer matrix or carrier for diagnostic purposes was suggested based on findings in this part.

Part 2 is the main part of this research. This part synthesised and characterised different formulations (v/v%) of Er₂O₃ nanoparticles embedded in a recommended wt% of PEO matrix (in Part 1) using the electrospinning technique. Furthermore, cellular evaluation of the PEO/Er₂O₃ nanofibres comprised cytotoxicity study and functional characterisation using colony formation assay supplemented with the EFTEM analysis of monitoring the morphological changes in the human breast cancer cell line (MCF-7) was carried out. The ideal PEO/Er₂O₃ nanofibre formulation for diagnostic purposes was suggested in this part.

Part 3 is the application part of this research. The parameterisation resonance of Er_2O_3 nanoparticles and PEO/ Er_2O_3 nanofibres, including the internalisation of these samples in MCF-7 cells, was performed for T1- and T2-weighted image measurements using MRI 1.5 Tesla. The suitability of PEO/ Er_2O_3 nanofibres either to be positive (T1) or negative (T2) diagnostic agents was determined based on their relaxivity enhancement (r_1 or r_2). Further assessment of a dose concentration *in vitro* MRI was carried out to evaluate the sensitivity of PEO/ Er_2O_3 nanofibres as dose concentration-dependent for effective diagnostic agents.

1.5 Significance of the study

Although the development of diagnostic agents for MRI has achieved great success, single-mode (T1 or T2) diagnostic agents have advantages and limitations. A potential strategy was to develop a T1-T2 dual-mode diagnostic agent to improve the detection sensitivity since combining both modes can cross-validate the obtained image data, yielding complementary and self-confirmed information for sensitive and accurate MRI. The beneficial contrast effects are two-fold: T1 imaging provides high tissue resolution, whereas T2 imaging provides high feasibility in disease detection. Therefore, the scientific findings in this research contribute to developing a forthcoming T1-T2 dual-mode diagnostic agent in nanofibres form for bioimaging modalities, specifically in MRI. Additionally, T1-T2 dual-mode diagnostic nanofibres are a relatively new advanced diagnostic agent expected to improve the relaxation rate.

1.6 Dissertation outline

This dissertation comprises five chapters as follows:

Chapter 1 (Introduction) briefly justifies the background of the study and the benchmark in this research. The problem statement arose from the current benchmark

and subsequently found the alternative for the drawbacks. Research objectives and scope of the study are available in this chapter, including the study's significance and the dissertation outline.

Chapter 2 (Background, Theory and Literature review) describes diagnostic imaging, especially MRI. This chapter clarifies the basic principle of MRI, the type of diagnostic agents, electrospinning, and the physical and chemical properties of PEO and Er₂O₃ nanoparticles. This chapter also provides the basic knowledge of *in vitro* studies using the MCF-7 breast cancer cell line.

Chapter 3 (Materials and Methods) elaborates on the methodology of synthesising PEO and PEO/Er₂O₃ polymer blends into polymeric fibres for diagnostic use. The nanofibres were fully characterised with physical characterisation, including the *in vitro* study using MCF-7 breast cancer cell line and resonance parameterisation of MRI.

Chapter 4 (Results and Discussion) discusses the scientific findings discovered from the characterisation results and their detailed explanations.

Chapter 5 (Conclusion and Recommendation) summarises the research findings and contributions to the medical imaging field's development as a diagnostic agent. Finally, this chapter presents future work recommendations for better outcomes and reliable scientific discoveries to improve this research.

CHAPTER 2

THEORY AND LITERATURE REVIEW

2.1 Introduction to diagnostic imaging

Diagnosis means identifying an illness by examining the symptoms and signs. Diagnostic imaging describes the visual techniques to recognise an illness by examining the human body and investigating the causes. This technique helps medical practitioners to have a better understanding of the patient's conditions. There are many distinguished techniques in diagnostic imaging (e.g., magnetic resonance imaging (MRI), mammography, nuclear magnetic resonance (NMR), X-ray, ultrasound, and computed tomography (CT) scan). MRI was the main focus of this work as the diagnostic imaging technique because of its suitability for *in vitro* cancer research.

2.2 Principles of magnetic resonance imaging (MRI)

Magnetic resonance imaging (MRI) specialises in soft tissue examination with wide availability and has provided anatomical images with high spatial and temporal resolution without harmful radiation since the 1980s. MRI focuses on one type of atomic nucleus. This nucleus refers to hydrogen proton (^1H proton) in water inside the human body. The ^1H proton is a charged sphere that rotates with a magnetic moment and collinear angular momentum. These two entities are quantified in terms of magnetic and spin quantum numbers.

MRI operates with a powerful magnet that spins rapidly to change the magnetic fields that, in turn, induce the relaxation of ^1H protons. Since the human body consists of approximately 60% water, the ^1H protons in the human body are forced to align with the changes in the magnetic field and simultaneously produce an image. A

diagnostic agent can enhance the MRI image by increasing the speed of the ^1H protons to align. The faster the protons realign, the brighter the image.

2.2.1 T1 longitudinal relaxation time

The T1 longitudinal or spin-lattice relaxation time is characterised by the speed of the net magnetisation vector (\mathbf{M}_z) returning to equilibrium in the direction of the external magnetic field (\mathbf{B}_0) derived from the Bloch equation:

$$\frac{\delta M_z(x)}{d\delta} = \frac{M_0 - M_z(t)}{T1} \quad [2.1]$$

This parameter is defined as the time required for M_z to recover approximately 63% of its equilibrium value after applying a radiofrequency (RF) pulse. \mathbf{M}_0 refers to equilibrium magnetisation. At this time, the excited electron (spin) releases its absorbed energy back to its surrounding lattice, creating a thermal equilibrium. Thus, the behaviour of the T1 relaxation time follows the equation:

$$M_z(t) = M_0(1 - e^{-\frac{TR}{T1}}) \quad [2.2]$$

\mathbf{M}_z is the magnetisation at $t = 0$, whereas \mathbf{M}_0 is the initial maximum value at full recovery along the z-axis. The spins are relaxed after $t \gg 5 T1$ times. A schematic diagram of T1 longitudinal relaxation time is depicted in Figure 2.1.

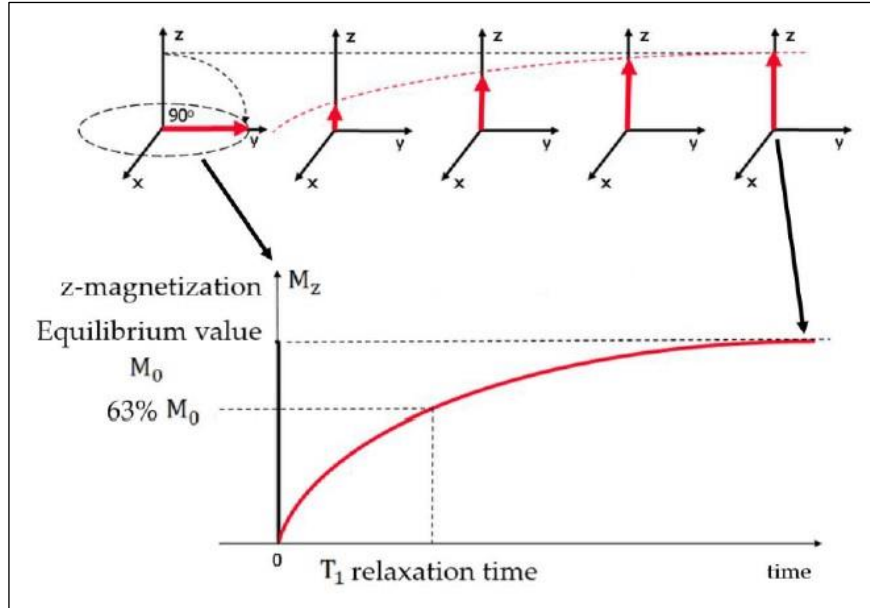


Figure 2.1 Schematic diagram of T1 longitudinal relaxation time after applying 90° RF pulse to the MRI system at equilibrium. The net magnetisation vector of the z-axis (M_z) is reduced to zero but gradually returns to its equilibrium value without the RF pulse (Caspani et al., 2020).

2.2.2 T2 transverse relaxation time

The transverse or spin-spin relaxation time (T2) is characterised by the absence of any radiofrequency (RF) field of the net magnetisation vector (\mathbf{M}_{xy}) in the direction of the external magnetic field (\mathbf{B}_0) derived from the Bloch equation:

$$\frac{\delta M_{xy}(t)}{d\delta} = \frac{M_{xy}(t)}{T2} \quad [2.3]$$

This parameter is the interval during which transverse magnetisation decreases to approximately 37% of its value. The RF pulse is applied in the presence of longitudinal magnetisation, thus generating a transverse magnetisation. Consequently, the signal experiences dephasing of the M_0 , followed by the elimination of the RF pulse (B_0) of 90°. The dephasing is principally due to the energy transfer between spins (spin-spin interactions) and time-dependent inhomogeneities of the B_0 (Bojorquez et al., 2017). A schematic diagram of T2 transverse relaxation time is portrayed in Figure 2.2.

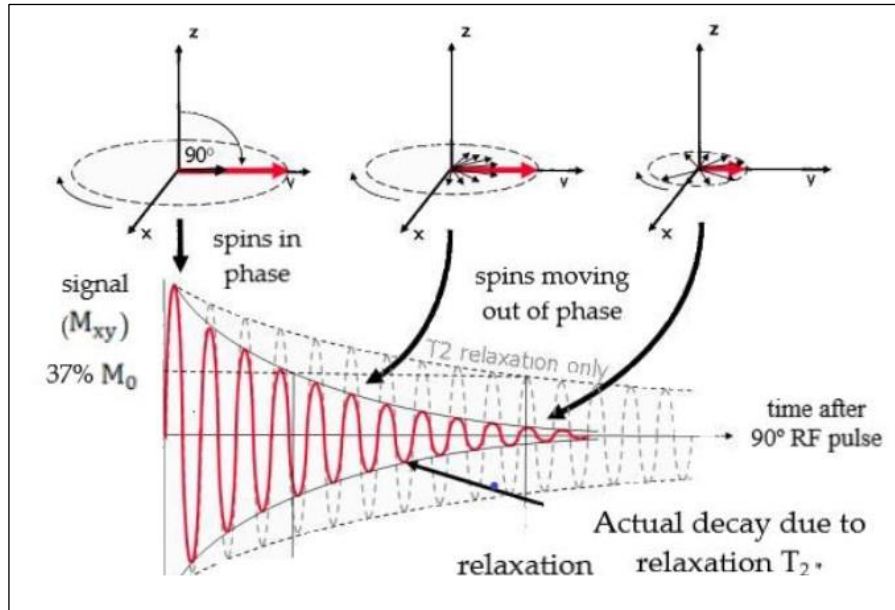


Figure 2.2 Schematic diagram of T2 transverse relaxation time after applying 90° RF pulse to the MRI system at equilibrium. Initially, the transverse magnetisation (red arrow) has a maximum amplitude as the population of magnetic moments rotates in phase towards the xy plane. The amplitude of the net transverse magnetisation decays without the RF pulse. Free Induction Decay (FID) is the resultant decay signal (Caspani et al., 2020).

By forming a spin echo (after a 180° RF), some sources of decay are reversed, and an exponential decay governs the amplitude of the spin echo:

$$M_{xy}(TR, TE) = M_0(1 - e^{-\frac{TR}{T_1}}) \left(e^{-\frac{TE}{T_2}} \right) \quad [2.4]$$

TR is the repetition time, whereas **TE** is the echo time. **M₀** refers to equilibrium magnetisation, **T₁** is the longitudinal relaxation time, and **T₂** is the transverse relaxation time. If a $TR \gg 5 T_1$ is used, then the equation changes to its simplest form:

$$M_{xy}(TE) = M_0 e^{-\frac{TE}{T_2}} \quad [2.5]$$

2.3 Diagnostic agents

The relaxation time of normal and abnormal tissues may be similar during MRI diagnosis. Therefore, a diagnostic agent (contrast agent) is needed to effectively

enhance the MRI image of the small metastasis before proceeding to a specific treatment. A diagnostic agent aims to accelerate the water protons in the surrounding tissues to enhance signal contrast and improve image resolution for the visibility of structures within the body for medical examination. This agent is usually given to patients by intravenous or non-intravenous (oral consumption or rectal administration) before medical examination under medical imaging modalities such as MRI, CT scan, ultrasound, mammography, and many more. A diagnostic agent usually contains paramagnetic metal ion complexes or superparamagnetic magnetite particles due to their relaxivity (ability to increase the relaxation rate of water protons spins in a diagnostic agent concentration-dependent manner). Consequently, these elements shorten T1 and T2 relaxation times, thus causing an increment in signal intensity on T1-weighted images or a reduction in signal intensity on T2-weighted images.

There are two types of diagnostic agents, which are positive and negative diagnostic agents. Positive diagnostic agents shorten the T1 relaxation time, causing enhanced parts to appear bright on T1-weighted images. Meanwhile, negative diagnostic agents shorten T2 relaxation time, causing enhanced parts to appear darker on T2-weighted images. MRI diagnostic agents interact with H₂O protons and either modify their relaxation times or are directly involved in the level of H₂O proton magnetisation. The first established MRI diagnostic agent was ferric chloride for the gastrointestinal (GI) tract, introduced in 1981, followed by using gadolinium compound as an intravascular diagnostic agent in 1984 (Carr et al., 1984; Young et al., 1981).

Recent advancements have used polymer to design a diagnostic agent. A polymer diagnostic agent is also incorporated to shorten water molecules of T1 and T2 relaxation times adjacent to the polymer. The contrast effect is improved when one

tissue has either a higher affinity for the diagnostic agents or higher vascularity than another. Cancers or abnormal cells have different metabolisms from healthy tissues and tend to take up the diagnostic agent differently, resulting in a contrast effect in MRI images. The T1-weighted image shows anatomy with a clear structure image, whereas the T2-weighted image provides good pathological information since abnormal fluid appears brighter than the normal tissue background. However, nearly all MRI diagnostic agents affect T1- and T2-weighted images. The effects of diagnostic agents in improving the signal intensity of those images are categorised as either T1 or T2 diagnostic agents.

The relaxation rate is (**R**) used to measure the contrast enhancement using the following equation:

$$R_n = \frac{1}{T_n} \quad n = 1 \text{ or } 2 \text{ (unit: s}^{-1}\text{)} \quad [2.6]$$

Meanwhile, the relaxivity (**r**) is used to define the efficiency of a diagnostic agent with the following equation:

$$r_n = \frac{R}{C_{DA}} \quad n = 1 \text{ or } 2 \text{ (unit: mM}^{-1}\text{s}^{-1}\text{)} \quad [2.7]$$

C_{DA} is the analytical ion concentration of the diagnostic agent. The efficiency of a diagnostic agent was evaluated using the r_2/r_1 ratio. A r_2/r_1 ratio of T1 diagnostic agent is less than 5 ($r_2/r_1 < 5$), whereas a r_2/r_1 ratio of T2 diagnostic agent is more than 10 ($r_2/r_1 > 10$). Meanwhile, the diagnostic agent can be categorised as a T1-T2 dual-mode diagnostic agent when the r_2/r_1 ratio is between 5 and 10 ($5 < r_2/r_1 < 10$). The relaxivity also depends on the magnetic field and temperature.

The observed water relaxation rate (r_{obs}) increased by 1 mmol.L⁻¹ of active ions in the diagnostic agent, referred to as the relaxivity for an MRI diagnostic agent using the equation (Swartjes et al., 2022):

$$r_{n,\text{obs}} = \frac{\left[\frac{1}{T_{n,\text{obs}}} - \frac{1}{T_{n,\text{water}}} \right]}{C_{\text{DA}}} \quad n = 1 \text{ or } 2 \text{ (unit: mM}^{-1}\text{s}^{-1}\text{)} \quad [2.8]$$

2.3.1 Positive (T1) diagnostic agent

A positive diagnostic agent shortens the longitudinal relaxation time of water protons (T1), producing hyperintense signals in T1-weighted images. Consequently, the affected regions have a brighter contrast effect with these agents. An example of a positive diagnostic agent is Gadolinium (Gd). Gd has been a diagnostic agent for decades due to its ideal proton relaxation properties. It is one element in the lanthanide group with a strong paramagnetic property. Paramagnetism is an intrinsic property of a specific material that temporarily becomes magnetised under an external magnetic field. It plays a significant role in improving the image quality at the target site under examination. However, free Gd³⁺ ions are inherently toxic and must be administered in their stable form to prevent the release of metal ions. Still, Gd is a concern for clinical use due to its high toxicity level (Wysokińska et al., 2019).

Free Gd³⁺ ions are 50 times higher than chelated Gd (Cacheris et al., 1990; Ersoy and Rybicki, 2007). For this reason, researchers worldwide focus on improving Gd-based diagnostic agents (Gadolinium-based contrast agents (GBCAs)). These agents comprise a Gd³⁺ ion (metal ion) bonded with another carrier molecule known as a chelating agent to prevent Gd's toxicity while maintaining its contrast characteristics. There are two types of chelating agents, known as macrocyclic and

linear, binding with Gd^{3+} ions for their stability and to minimise toxicity (Malikova and Holesta, 2017; Rees et al., 2018; Tyler et al., 2017).

Using Gd(III) complexes as diagnostic agents in MRI has proven to be the most valuable in diagnosing several internal abnormalities. However, chronic cases occurred in 1997 whereby patients with impaired renal function developed nephrogenic systemic fibrosis (NSF) disease, followed by several cases in 2016 of Gd accumulation throughout the body, including in the brain, in patients with normal renal function, caused by a higher T1 signal on unenhanced T1-weighted images located in the globus pallidus and dentate nucleus. Since then, prolonged exposure to GBCAs has been considered unsafe. Moreover, GBCAs can induce mitochondrial toxicity and death in human neurons. The morbidity associated with NSF can include severe pain and immobility and even cause death in some cases (Garcia et al., 2017; Hojreh et al., 2020; Layne et al., 2018; Le Fur and Caravan, 2019; Mallio et al., 2020; Olchoway et al., 2017; Pasquini et al., 2018; Ranga et al., 2017; Rozenfeld and Podberesky, 2018; Seta et al., 2019). For this reason, the European Medicines Agency (EMA) has recommended limits and suspensions for specific intravenous linear agents (European Medicines Agency, 2017) to eliminate complications associated with Gd deposition in the brain.

Magnevist or Gd-DTPA (Gd-diethylenetriaminepentaacetate) is commonly used as a T1 diagnostic agent because it can shorten the T1 longitudinal relaxation time of water protons and increase the image contrast. However, due to its low molecular weight, it has disadvantages such as a lack of specificity to target organs and tissue for diagnosis and a short half-life in the blood. Therefore, many diagnostic agents are administered to the patient by injection before the examination.

2.3.2 Negative (T2) diagnostic agent

A negative diagnostic agent reduces the water proton's transverse relaxation time (T2), causing hypointense signals or darker images in T2- and T2*-weighted images. The phenomenon was caused by the enormous magnetic field heterogeneity surrounding the diagnostic agent through which water molecules diffused, as diffusion causes dephasing of the proton magnetic moments, consequently shortening the T2 transverse relaxation time. A T2 diagnostic agent is also known as a susceptibility agent because of its effect on the magnetic field. T1 shortening requires a close interaction between water molecules and the T1 diagnostic agent, whereas T2 shortening is a distant effect. Another difference with T1 diagnostic agents is that R_2 (transverse relaxation rate) tends asymptotically to a positive constant under high magnetic fields.

T2 diagnostic agents are usually superparamagnetic nanoparticles and ferromagnetic nanoparticles. Among established T2 diagnostic agents, superparamagnetic iron oxide nanoparticles (SPIONs) have been effectively employed for cell labelling or tumour detection and image-guided diagnosis using MRI in clinical practice (Barrow et al., 2018; Bulte, 2019; Chandrasekharan et al., 2020; Lazaro-Carrillo et al., 2020; Ohki et al., 2020; Vangijzegem et al., 2020). SPIONs can also generate reactive oxygen species (ROS), both intrinsically or when activated using various stimuli (Dadfar et al., 2020; Duan et al., 2019; Khaniabadi et al., 2020; Sharkey et al., 2017; Wang et al., 2021). Due to these intriguing features, SPION is adaptable for cancer diagnosis (Tong et al., 2019; Vangijzegem et al., 2023; Zhi et al., 2020).

SPIONs are nanocrystals of iron oxide, either magnetite (Fe_3O_4) or maghemite ($\gamma\text{-Fe}_2\text{O}_3$), typically ranging from 5 nm to 150 nm in diameter. Their surfaces are specifically modified to promote stability in aqueous environments. This also provides

desired biochemical properties, including magnetic sensitivity and performance, enabling their application as MRI diagnostic agents (Chen et al., 2022; Dulińska-Litewka et al., 2019). SPIONs have high detection sensitivity for lesions from surrounding normal tissues (Waddington et al., 2020).

In addition, SPIONs can be conjugated with various targeting moieties, including antibodies, transferrin, aptamers, hyaluronic acid, folate and targeting peptides. These allow recognition by specific receptors that are selectively overexpressed on the targeted tumour cells, resulting in reduced off-target effects (Dadfar et al., 2019; Duan et al., 2019; Frantellizzi et al., 2020; Zhi et al., 2020). Due to their magnetic properties, SPIONs can respond specifically to either high- or low-frequency alternating magnetic fields. This enables their use in magnetic hyperthermia or magnetic-mechanical therapies.

However, SPION-based diagnostic agents face challenges such as insufficient tumour accumulation and low contrast performance. This stems from their magnetic susceptibility artefacts and inherent dark contrast effects, which restrict their usage by inducing poor signal-to-noise ratios. Consequently, it is difficult to distinguish the region of the signal induced by SPION from a low-level background of signals, such as signals arising from adjacent tissues, bone or vasculature. Therefore, it makes the sensitivity for pathological diagnosis slightly poor (Cheheltani et al., 2016; Dulińska-Litewka et al., 2019; Polu and Rhee, 2016).

Moreover, studies have shown SPIONs cytotoxic impacts on developing umbilical vein endothelial cells (HUVECs), melanoma cells, and human neurons, suggesting their toxicology should not be underestimated (Naumenko et al., 2018; Vakili-Ghartavol et al., 2020). A major toxic effect of SPIONs is their potential to generate reactive oxygen species (ROS), putting cells through oxidative stress. Free

ferrous ions (Fe^{2+}) from SPIONs can also react with mitochondrial oxygen and hydrogen peroxide *via* the Fenton reaction. These are very highly reactive biomaterials that may cause damage to the DNA, lipids, proteins, and polysaccharides in cells due to the production of ferric ions (Fe^{3+}) and hydroxyl radicals (Nelson et al., 2020).

Since the first FDA approval of a SPION-based diagnostic agent in 1996, several similar products emerged but were later discontinued over safety concerns related to impaired mitochondrial function, apoptotic bodies, reactive oxygen species (ROS) generation, and DNA damage (e.g., Resovist, Lumirem, and Feridex). Currently, the sole Food and Drug Administration (FDA) approved product is Ferumoxytol, used off-label for MRI and angiography in renal failure patients beyond its approved indication for iron-deficiency anaemia treatment in chronic kidney disease (Dulińska-Litewka et al., 2019; Frantellizzi et al., 2020; Lazaro-Carrillo et al., 2020).

2.4 Introduction to electrospinning

Electrospinning (ES) is an effective and adaptable method to generate a one-dimensional (1D) fibre structure characterised by its diameter size from nanometre to micrometre, which is beneficial in various applications. This method has gained tremendous scientific and industrial interest due to its cost-efficiency, large surface area-to-volume ratio, versatility, ease of functionalisation, tailored porosity, excellent mechanical and physicochemical properties, and simplicity (Asghari et al., 2020; Bahnson et al., 2016; Calzoni et al., 2019; Haider et al., 2018; Jin et al., 2016; Morgan et al., 2016; Piotrowska et al., 2018; Prabhu, 2019; Topuz and Uyar, 2019).

Electrospun fibres have been widely explored and applied in tissue engineering, drug delivery, and diagnosis because the ES offers unprecedented control

over the resultant nanofibrous structure and the capability to encapsulate various organic and inorganic materials (Chen et al., 2022; Homaeigohar and Boccaccini, 2020; Zhao and Cui, 2020). Electrospun nanofibres have recently emerged as a promising sensing platform for cancer diagnostic and bioanalytes, including nucleic acids and gene sequences, hormones, superoxide anions, proteins, and even circulating cancer cells (Hernández and Chauhan, 2020). Previous studies proved that the ES method could improve the distribution of nanoparticles within the polymer matrix and enhance the properties of nanocomposites (Wu et al., 2020). Therefore, this is a reliable method for this research.

2.5 Principles of electrospinning system

The electrospinning technique is used to fabricate fibres from polymers. In the ES method, the fibres are formed from a fluid or melt (polymer blend) through electrohydrodynamic processes facilitated by a high-voltage power supply. A schematic illustration of the conventional setup of the ES system consists of a syringe pump, a syringe attached to a spinneret (hypodermic or blunt needle), a metal collector (positioned vertically or horizontally), and applied high voltage, as provided in Figure 2.3.

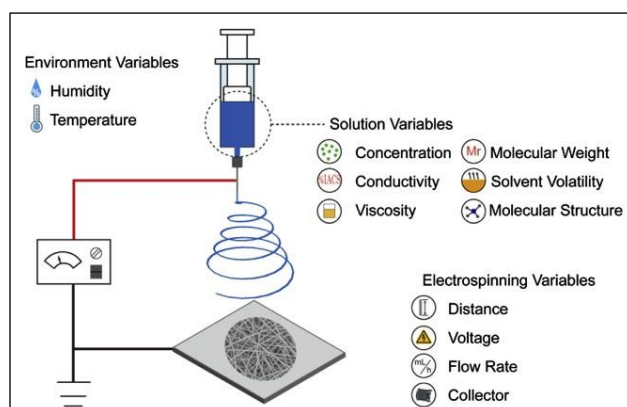


Figure 2.3 Schematic illustration of the conventional electrospinning (ES) setup and its variable parameters (Long et al., 2018).